Geophysical Journal International

Geophys. J. Int. (2023) **235,** 831–852
Advance Access publication 2023 July 08
GJI Seismology

https://doi.org/10.1093/gji/ggad278

Cascading foreshocks, aftershocks and earthquake swarms in a discrete fault network

Kyungjae Im and Jean-Philippe Avouac

Geology and Planetary Science Division, California Institute of Technology, Pasadena, CA 91125, United States. E-mail: kjim@caltech.edu

Accepted 2023 July 2. Received 2023 June 19; in original form 2022 July 13

SUMMARY

Earthquakes come in clusters formed of mostly aftershock sequences, swarms and occasional foreshock sequences. This clustering is thought to result either from stress transfer among faults, a process referred to as cascading, or from transient loading by aseismic slip (pre-slip, afterslip or slow slip events). The ETAS statistical model is often used to quantify the fraction of clustering due to stress transfer and to assess the eventual need for aseismic slip to explain foreshocks or swarms. Another popular model of clustering relies on the earthquake nucleation model derived from experimental rate-and-state friction. According to this model, earthquakes cluster because they are time-advanced by the stress change imparted by the mainshock. This model ignores stress interactions among aftershocks and cannot explain foreshocks or swarms in the absence of transient loading. Here, we analyse foreshock, swarm and aftershock sequences resulting from cascades in a Discrete Fault Network model governed by rate-and-state friction. We show that the model produces realistic swarms, foreshocks and aftershocks. The Omori law, characterizing the temporal decay of aftershocks, emerges in all simulations independently of the assumed initial condition. In our simulations, the Omori law results from the earthquake nucleation process due to rate and state friction and from the heterogeneous stress changes due to the coseismic stress transfers. By contrast, the inverse Omori law, which characterizes the accelerating rate of foreshocks, emerges only in the simulations with a dense enough fault system. A high-density complex fault zone favours fault interactions and the emergence of an accelerating sequence of foreshocks. Seismicity catalogues generated with our discrete fault network model can generally be fitted with the ETAS model but with some material differences. In the discrete fault network simulations, fault interactions are weaker in aftershock sequences because they occur in a broader zone of lower fault density and because of the depletion of critically stressed faults. The productivity of the cascading process is, therefore, significantly higher in foreshocks than in aftershocks if fault zone complexity is high. This effect is not captured by the ETAS model of fault interactions. It follows that a foreshock acceleration stronger than expected from ETAS statistics does not necessarily require aseismic slip preceding the mainshock (pre-slip). It can be a manifestation of a cascading process enhanced by the topological properties of the fault network. Similarly, earthquake swarms might not always imply transient loading by aseismic slip, as they can emerge from stress interactions.

Key words: Computational seismology; Earthquake hazards; Earthquake interaction, forecasting, and prediction; Statistical seismology.

1. INTRODUCTION

Earthquake clusters are abundant in seismicity catalogues. They can consist of mainshock–aftershock sequences, foreshock sequences or swarms (Mogi 1963). Aftershocks are most common and easily observable in regular earthquake catalogues. Swarms resemble aftershock sequences but do not have a mainshock and are often inferred to be associated with transient aseismic slip (e.g. Vidale & Shearer 2006; Lohmann & McGuire 2007; Llenos *et al.* 2009; Ross *et al.* 2017; Sirorattanakul *et al.* 2022), and fluid flow (e.g. Ross *et al.* 2020). Foreshocks are less frequent but can still be detected in regular seismicity catalogues (e.g. Jones & Molnar 1979; Bouchon *et al.* 2013; Chen & Shearer 2016; Kato & Ben-Zion 2021). They have frequently been observed prior to subduction interplate

earthquakes (e.g. Bouchon *et al.* 2013; Ruiz *et al.* 2014; Kato & Ben-Zion 2021). They might actually not be uncommon in other settings. For example, the analysis of an enhanced seismicity catalogue obtained with template matching techniques (Ross *et al.* 2019a) has shown that, in California, more than 20 per cent of $M > 4$ earthquakes have foreshocks, even though their precise proportion has been debated (Trugman & Ross 2019; van den Ende & Ampuero 2020; Moutote *et al.* 2021).

Aftershocks are well understood to be triggered either directly by the mainshock (Dieterich 1994) or indirectly via other aftershocks (e.g. Ziv & Rubin 2003; Marsan 2005; Marsan & Lengliné 2008; Cattania *et al.* 2015), afterslip (e.g. Perfettini & Avouac 2004; Cattania *et al*. 2015; Frank *et al.* 2017) or possibly pore pressure diffusion (Nur & Booker 1972; Miller *et al.* 2004). Spatially, aftershocks correlate primarily with the Coulomb stress changes from mainshock (e.g. King *et al.* 1994; Harris 1998) and would therefore be consistent with direct triggering. However, indirect triggering, and possibly afterslip, are probably also playing a role, as implied by the gradual expansion of aftershocks with time (e.g. Ziv & Rubin 2003; Marsan 2005; Perfettini & Avouac 2007; Marsan & Lengliné 2008; Peng & Zhao 2009; Perfettini *et al.* 2018), and the occurrence of aftershocks in zones of negative Coulomb stress change (often called 'stress shadows') due to the mainshock (Marsan 2006; Ziv 2006; Meier *et al.* 2014).

It is well established that the rate of aftershocks decays with time following $1/t^p$ with $p \sim 1$, called the Omori law for $p = 1$, or the modified Omori law for $p \neq 1$ (Omori 1894; Utsu *et al.* 1995). This phenomenological law can be explained as the result of the time-dependent earthquake nucleation process derived from laboratory-based rate and state friction (Dieterich 1979). Although aftershocks could also be governed by pore-pressure changes (e.g. Nur & Booker 1972) or afterslip (e.g. Perfettini & Avouac 2004), this prediction is considered a success in support of the rate and state theory of earthquake nucleation (e.g. Dieterich 1994). The spatial distribution of aftershocks is generally well explained with static stress triggering (King *et al.* 1994). The 'Coulomb rate and state (CRS) model' (Stein *et al.* 1997; Ziv & Rubin 2003; Helmstetter & Shaw 2006; Heimisson & Segall 2018; Ozawa & Ando 2021) combines the two elements to predict the resulting process in time and space. Despite its well-established foundations and the success of the CRS model at explaining qualitatively and quantitatively aftershocks sequences (e.g. Stein *et al.* 1997), statistical models such as the Epidemic-Type Aftershock Sequence (ETAS) model (Kagan & Knopoff 1981; Ogata 1988; 1998) actually tend to predict better the spatiotemporal evolution of aftershocks, probably because of their ability to capture the effect of heterogeneities and clustering (e.g. Llenos *et al.* 2009; Segou *et al.* 2013; Cattania *et al.* 2014; Mancini *et al.* 2019; Hardebeck 2021). Note that, when the CRS model is applied to real cases, indirect triggering by aftershocks is generally ignored because it would require detailed knowledge of the slip distribution due to each aftershock which is impractical. The cascading process can, however, be incorporated into numerical simulations based on rate and state friction (Ziv 2003; Ziv & Rubin 2003; Dieterich & Richards-Dinger 2010; Ozawa & Ando 2021; Dublanchet 2022). Such simulations have been found to reproduce foreshock and aftershock statistics, in particular, the Omori and inverse Omori laws (Dieterich 1994; Ziv & Rubin 2003; Dieterich & Richards-Dinger 2010; Richards-Dinger & Dieterich 2012). However, these simulations did not explore the role of secondary faults. Secondary faults are observed to be systematically associated with major faults forming fault zones with rather complex fault geometries (e.g. Faulkner *et al*. 2010; Savage & Brodsky 2011). They probably play an important role in generating foreshocks and aftershocks. Ozawa & Ando (2021) considered secondary faults and analysed their contribution to aftershocks, but they didn't investigate foreshocks.

Foreshocks might result from the same cascading process as aftershocks (Ellsworth & Bulut 2018). In this view, foreshocks and aftershocks result from the same interevent triggering process: a mainshock is simply an earthquake triggered by a previous event, which happens to be of lower magnitude and therefore dubbed a foreshock in retrospect. For example, the M 7.1 mainshock of the 2019 Ridgecrest earthquake sequence occurred within the aftershocks sequence of a previous M 6.4 foreshock (Ross *et al.* 2019b; Chen *et al.* 2020; Lomax 2020). Numerical simulations of cascading based on ETAS (Helmstetter & Sornette 2002) or the CRS model (Ziv 2003; Dieterich & Richards-Dinger 2010) can indeed produce foreshock sequences. Such simulations can explain the observation that, if multiple sequences of foreshocks are stacked, they follow an 'inverse Omori law', meaning a power-law acceleration of seismicity rate similar to aftershocks sequence but reverse in time (Jones & Molnar 1979). An alternative view to the cascade model is that foreshocks would be driven by pre-slip, aseismic slip preceding the mainshock. There are examples of foreshock sequences associated with transient geodetic deformation in support of that view (e.g. Kato *et al.* 2012; Ruiz *et al.* 2014). According to this view, foreshocks are a by-product of aseismic slip associated with pre-slip, eventually due to the mainshock nucleation process. In recent years, several examples of large mainshocks preceded by foreshocks sequence were well documented. Some foreshock sequences can be better explained by the pre-slip model than the cascade model (Dodge *et al.* 1996; McGuire *et al.* 2005; Kato *et al.* 2012; Bouchon *et al.* 2013; Ruiz *et al.* 2014; Tape *et al.* 2018). Conversely, some other recent observations favour the cascade model (Ellsworth & Bulut 2018; Yoon *et al.* 2019; Lomax, 2020). A nucleation model involving pre-slip-driven and cascading foreshocks is actually plausible (Kato & Ben-Zion 2021) and is supported by laboratory experiments (McLaskey 2019) and numerical simulations (Cattania & Segall 2021). These different views are thus not necessarily exclusive.

Because geodetic measurements of pre-slip are rarely available, the possibility of pre-slip is often estimated by testing the fraction of observed foreshocks against the prediction for a cascading process assumed to result from static coseismic stress transfer. Because of its superior performance at matching aftershocks, ETAS is generally used to assess this probability (e.g. McGuire *et al.* 2005; Bouchon *et al.* 2013 Moutote *et al.* 2021). The ETAS model often predicts much fewer foreshocks than observed. This is documented on oceanic transform faults (McGuire *et al.* 2005), subduction zones (Bouchon *et al.* 2013), and to a lesser extent, in the context of the San Andreas fault system in Southern California (Moutote *et al.* 2021). Assuming that ETAS correctly predicts foreshocks due to cascading, it follows that pre-slip would be needed to explain the abundance of foreshocks. There is, however, no assurance that it is appropriate to use ETAS for that purpose. First, ETAS is additive and unbounded although, in reality, (1) clustering probably results from a time-advance process (e.g. Stein 1999; Gomberg 2001), (2) the moment release must be bounded by the initial stress and the rate of loading due to tectonics and (3) large faults are generally embedded in a complex fault zone with secondary faults and fractures associated with the main fault (e.g. Ben-Zion & Sammis 2003). The density of secondary faults and fractures is dependent on the magnitude of cumulated fault slip and decaying with distance away from the main fault (Faulkner *et al.* 2010; Savage & Brodsky

2011). A higher fault density around the major faults should favour fault interactions and boost the fraction of foreshocks. Therefore, this study aims to analyse the cascading process in synthetic earthquake sequences generated in a network of faults obeying rate and state friction, analyse the predicted sequences of foreshocks and aftershocks and compare our modelling results with the cascading process in ETAS simulations.

Hereafter we first present an analytical approximation of the time evolution of foreshocks dues to cascading. This analysis builds in particular on the studies of Dieterich (1994), Heimisson & Segall (2018) and Heimisson (2019). We then present numerical simulations for a discrete fault network following an approach similar to that of Ozawa & Ando (2021), Dublanchet (2022), or the inherently discrete fault model of Ziv (2003) and Richards-Dinger & Dieterich (2012). We consider fault networks with varied complexity and investigate the influence on foreshocks and aftershocks. The simulation results are compared with the statistical characteristics of seismicity catalogues, including the Omori law, the inverse Omori law, and the Gutenberg–Richter law. The stacked foreshock and aftershock rates are further compared with the prediction from the ETAS model.

2. INTERACTIONS IN A NETWORK OF FAULTS GOVERNED BY RATE AND STATE FRICTION—THEORY

This section briefly reviews rate and state friction and Dieterich (1994)'s model of aftershocks (Section 2.1). Then, the theory is adapted to foreshocks with account for source interactions (Section 2.2), and finally, the role of stress change heterogeneities is included (Section 2.3). The analytic expressions presented in this section are derived based on simplifying assumptions, which are relaxed in the numerical simulations presented in the following section.

2.1. Frictional framework and Dieterich model

Laboratory studies show that friction depends on the slip rate and on some state variable that allows restrengthening (also referred to as 'healing') at low slip rates (Dieterich 1979; Marone 1998). The most common form is

$$\mu = \mu_0 + A \log\left(\frac{V}{V_0}\right) + B \log\left(\frac{V_0\theta}{D_c}\right), \tag{1}$$

where V is velocity, θ is state variable, μ_0 is a reference friction coefficient at reference velocity V_0, D_c is a critical slip distance and A and B are empirical constants for the magnitude of direct and evolution effects, respectively.

The evolution of the state variable (θ) is commonly described using either of two widely used evolution laws denoted, respectively, as the ageing law (Dieterich 1979),

$$\frac{d\theta}{dt} = 1 - \frac{V\theta}{D_c}, \tag{2}$$

and the slip law (Ruina 1983),

$$\frac{d\theta}{dt} = -\frac{V\theta}{D_c} \log\left(\frac{V\theta}{D_c}\right). \tag{3}$$

The two evolution laws are similar when the system is near steady state ($\theta \sim D_c/V$) but substantially diverge otherwise. In the slip law, the state variable only evolves at non-zero velocity, whereas the ageing law delivers maximum healing in a static system ($V = 0$). Our simulations are conducted with the ageing law. However, we also conducted simulations with the slip law for comparison.

Dieterich (1994) presented an analytic expression for seismicity rate change by assuming a population of faults well-above-steady-state (meant to represent 'critically stressed' fault), $\theta >> D_c/V$. With this assumption, the ageing law (eq. 2) can be simplified to $\theta = \theta_0 e^{-\delta/\mathrm{Dc}}$, which allows deriving analytic expressions of seismicity rate change if the whole population is submitted to the same stress change. With this assumption, in a constantly loaded system with a loading rate $\dot{\tau}$, the rupture time (time to instability) is:

$$t_{\mathrm{inst}} = \frac{A\sigma_0}{\dot{\tau}} \log\left(\frac{\dot{\tau}}{HV_i\sigma_0} + 1\right), \tag{4}$$

where σ_0 is normal stress, V_i is initial velocity and

$$H = -\frac{k}{\sigma_0} + \frac{B}{D_c}, \tag{5}$$

where k is the stiffness of the fault.

Assuming a 'population' of non-interacting faults with initial conditions such that they would produce a constant seismicity rate for a constant loading rate, Dieterich (1994) showed that a step stress, representing the effect of a mainshock, results in an immediate increase of the seismicity rate followed by a $1/t$ decay consistent with the Omori law.

In the case that the normal, $\sigma(t)$, and shear stress, $\tau(t)$, vary with time in an unspecified way, Heimisson & Segall (2018) show that the rupture time can be obtained from the following equation

$$\int_0^{t_{\mathrm{inst}}} \exp\left(\frac{\tau(t')}{A\sigma(t')} - \frac{\tau_0}{A\sigma_0}\right) dt' = \frac{A}{HV_i}, \tag{6}$$

where V_i, τ_0 and σ_0 are the velocity, shear stress and normal stress at time $t = 0$, respectively. Heimisson & Segall (2018) further generalized eq. (6) as

$$\int_0^{t} \exp\left(\frac{S_a(t')}{A\sigma_0}\right) dt' = \int_0^{\mathrm{B}(N)} \exp\left(\frac{S_b(t')}{A\sigma_0}\right) dt', \tag{7}$$

where $S_a(t)$ is the stress change as a function of time and $S_b(t)$ is background (unperturbed) stressing, which is related to the time, t, to the instability of Nth source $\mathbf{B}(N)$.

2.2 Foreshock from interacting sources

In this section, we show that foreshock sequences can be explained based on the rate-and-state nucleation model used by Dieterich (1994) if fault interactions are considered. We use the mean-field approximation to represent stress interactions. We neglect tectonic loading, assuming that the period of time considered in this analysis is short enough that the influence of further tectonic loading is insignificant. This model predicts the emergence of inverse Omori law, which is often observed in stacked (i.e. averaged) foreshock sequences. More realistic numerical simulations are presented and discussed later in this work.

In nature, all faults interact with each other. If a sufficient number of critically stressed faults are located nearby, the interactions may significantly accelerate the event rate. To get a simple analytical expression, we assume a uniform and isolated population of interacting sources, which would produce a constant background seismicity rate [i.e. $\mathbf{B}(N) = N/r$ in eq. (7), where r is the background event rate] in the absence of a background stressing rate (i.e. $S_b = 0$). Hence, the right-hand side of eq. (7) becomes N/r.

To describe the stressing history S_a, resulting from source interactions, we make a mean-field approximation corresponding to a

uniform interaction model as suggested by Heimisson (2019). We define ΔS as the average stress change driven by a single seismic event on all other faults. Since the magnitude of the interaction between two faults is dependent on the fault distance, ΔS is dependent on the density of faults. If the fault density is high (the average distance is low), ΔS is high, and conversely, if the fault density is low (the average distance is high), ΔS is low. The stress change from the interactions is $S_a(t) = N(t) \times \Delta S$, where $N(t)$ is event count at time t. With the above simplifications, eq. (7) becomes

$$\int_0^t \exp\left(\frac{N(t')\Delta S}{A\sigma_0}\right)\mathrm{d}t' = \frac{N}{r}. \tag{8}$$

Solving the equation for N yields the number of events at time t. Eq. (8) has a solution

$$N = -rt_f \log\left(1 - \frac{t}{t_f}\right), \tag{9}$$

where the characteristic foreshock time

$$t_f = \frac{A\sigma_0}{r\Delta S}. \tag{10}$$

Differentiating eq. (9) yields that the seismicity rate, R, is given by

$$\frac{R}{r} = \frac{1}{1 - t/t_f}. \tag{11}$$

Eq. (11) predicts a hyperbolic increase of event rate as t approaches t_f (Fig. 1a), consistent with the inverse Omori law documented from stacking foreshock sequences observed in nature (Jones & Molnar 1979; Bouchon *et al.* 2013). The time at which the number of earthquakes due to the cascading process diverges, t_f, is inversely proportional to the average interaction stress ΔS, and therefore, the foreshock rate change is dependent on ΔS (Fig. 1b) and hence, on the density of the fault population. If the faults are packed closer, the average stress change ΔS increases, leading to a more rapidly diverging rate of foreshocks.

For a finite fault network (or finite accumulated stress), at some time before t_f (i.e. before R goes to infinite), the population of critically stressed faults should get depleted and the event rate should start decelerating. If no large event is triggered before the depletion, for instance, due to the absence of a large fault patch near the clustered event, the cluster would be characterized as a seismic swarm. If a large mainshock is triggered, it would significantly change the stress field in the area. Assuming that the stress change from the mainshock is significantly larger than interactions between smaller faults, the system departs from the prediction based on the mean-field approximation and prompts an aftershock sequence. Assuming that the mainshock occurred at time $t_m (< t_f)$, from eq. (11), the seismicity rate at the time before the mainshock t^* becomes

$$\frac{R}{r} = \frac{t_f}{t_f^* + t^*}. \tag{12}$$

with $t_f^* = t_f - t_m$ and $t^* = t_m - t$. It follows the inverse Omori law with respect to the arbitrarily selected mainshock time. The mainshock time t_m can be some arbitrary number smaller than t_f. The probability of a mainshock can be estimated, assuming that the frequency-magnitude distribution of earthquakes follows the Gutenberg–Richter law.

We consider two arbitrary cases of fault populations with different average interaction stress ΔS. One is dense, and therefore the interaction stress is large ($\Delta S = 2$ kPa), and the other is sparse, and therefore the interaction stress is small ($\Delta S = 100$ Pa). If both populations follow an identical Gutenberg–Richter law, statistically, they have the same chance of a mainshock rupture at a given cumulative event count N. We may assume that the mainshock occurs at some arbitrarily chosen value of N, for example, $N = 100$ or $N = 1000$. Given N, the mainshock time t_m can be calculated from eq. (9), and the seismicity rate can be calculated from eq. (11) (Fig. 1c). The densely populated case (red) shows a clear inverse Omori law trend for both values of N. Conversely, the sparsely populated case (blue) shows a weak ($N = 1000$) or no ($N = 100$) inverse Omori law trend (Fig. 1c).

One may consider a dimensionless mainshock time defined by the ratio between the mainshock recurrence time $\hat{t}_m$ and characteristic foreshock time t_f, which characterizes the hyperbolic increase of foreshocks. Because the expected occurrence time of the mainshock increases with its magnitude, it follows from eq. (12) that larger mainshocks are more likely to have notable foreshocks. From the Gutenberg–Richter law, the expected mainshock recurrence time $\hat{t}_m$ of earthquakes of magnitude larger than the mainshock magnitude M_m, is

$$\hat{t}_m = \frac{10^{b(M_m - M_c)}}{r}, \tag{13}$$

where r is the seismicity rate of earthquakes with a magnitude larger than a reference magnitude which could be chosen as the magnitude of completeness of the catalogue, M_c, and b is the Gutenberg–Richter b-value. With eqs (10) and (13), a dimensionless mainshock time can be defined,

$$\tau_m = \hat{t}_m / t_f = \frac{\Delta S 10^{b(M_m - M_c)}}{A\sigma}. \tag{14}$$

Eq. (14) quantifies the prospect of observing foreshocks. If $\hat{t}_m$ is much smaller than the characteristic foreshock time (i.e. small τ_m), the mainshock likely occurs well before t_f, and accordingly, the foreshock acceleration will be insignificant. For $A = 0.003$, $\sigma = 15$ MPa, $b = 1$, $M_c = 2$ and $M_m = 5$, the dimensionless mainshock time for $\Delta S = 100$ Pa and $\Delta S = 2$ kPa are $\tau_m(\Delta S = 100\ \text{Pa}) = 2.2$ and $\tau_m(\Delta S = 2\ \text{kPa}) = 44.4$. This result corresponds to Fig. 1(c) as the $\Delta S = 2$ kPa case (red) shows a more visible inverse Omori law than the $\Delta S = 100$ Pa case (blue). Eq. (14) predicts that the foreshock acceleration may be more easily seen for larger interaction ΔS, larger magnitude mainshock M_m and smaller normal stress system σ.

It should be noted that this analytical derivation does not imply that the inverse Omori law should be visible in an individual foreshock sequence. It would be observable only in a sequence including a large number of events, which is never the case in reality as detection is always limited. In the case of a small number of events, the aleatoric distribution of interevent time would mask the underlying statistical law. It is, therefore, a common practice in the analysis of real sequences or numerical simulation to stack individual sequences (e.g. Jones & Molnar 1979; Bouchon *et al.* 2013).

2.3 Aftershocks from heterogeneous stress change

Dieterich (1994) model assumes a 'population' of fault with a specific distribution of initial velocity so that a constant seismicity rate would result in a constant loading rate. This specific initial condition is actually not required to produce aftershock sequences consistent with the Omori law (Ziv 2003; Ozawa & Ando 2021). In the analysis presented in this section, we show that the Omori law can instead result from heterogeneous stress changes.

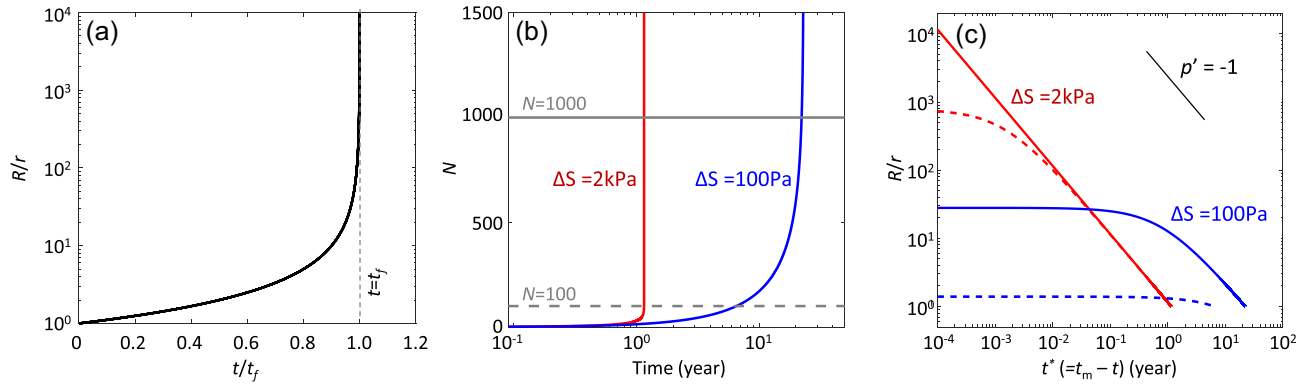

Figure 1. (a) Dimensionless seismicity rate versus dimensionless time (eq. 11). (b) Cumulative event number N with time (eq. 9) with different magnitudes of interaction (red $\Delta S = 2$ kPa, blue $\Delta S = 100$ Pa). Red and blue colours denote $\Delta S = 2$ kPa and $\Delta S = 100$ Pa cases, respectively. (c) Rate versus time before mainshock (eq. 12). The dashed line assumes that the mainshock occurred at $N = 100$, and the solid line assumes that the mainshock occurred at $N = 1000$. The dimensionless mainshock time is respectively $\tau_m(\Delta S = 100\ \text{Pa}) = 2.2$ and $\tau_m(\Delta S = 2\ \text{kPa}) = 44.4$.

In Dieterich's model, seismicity rate change during the aftershock sequence can be calculated from the impact of stress changes on time to instability (eq. 6). If a step shear and normal stresses change occurs at $t = 0$ in the absence of a background stressing rate, *i.e.* $\tau = \tau_0 + \Delta\tau$ and $\sigma = \sigma_0 + \Delta\sigma$, eq. (6) yields,

$$t_{\text{inst}} = \frac{A}{HV_i} \exp\left(\frac{\tau_0}{A\sigma_0} - \frac{\tau_0 + \Delta\tau}{A(\sigma_0 + \Delta\sigma)}\right). \tag{15}$$

Or approximately, assuming small stress changes compared to the initial stresses,

$$t_{\text{inst}} = \frac{A}{HV_i} \exp\left(-\frac{\Delta\sigma_f}{A\sigma_0}\right), \tag{16}$$

where $\Delta\sigma_f$ is Coulomb stress change defined as, $\Delta\sigma_f = \Delta\tau - \mu_0\Delta\sigma$ with $\mu_0 = \tau_0/\sigma_0$. Given the material properties H and A, eq. (16) shows that the time-to-instability of a well-above-steady-state (critically stressed) fault is determined by the magnitude of stress change ($\Delta\sigma_f$) and the velocity at the time (V_i).

Dieterich's model assumes that the faults form a 'population' that would produce a constant seismicity rate for a constant shear loading rate. This assumption requires a specific initial velocity distribution

$$V_i^N = \frac{\dot{\tau}}{H\sigma_0\left(\exp\left(\frac{N}{r}\frac{\dot{\tau}}{A\sigma_0}\right) - 1\right)}. \tag{17}$$

where V_i^{N} is the initial velocity of Nth event, $\dot{\tau}$ is the loading rate, r is the corresponding seismicity rate. Dieterich model additionally assumes that all the faults in a population experience an identical stress change. If the stress change is a step function, the Omori law naturally results from the time-to-instability change. Meanwhile, if the distribution of initial velocity does not follow eq. (17), the Omori law would not result from a step stress change. Although the constant seismicity rate at the constant stressing rate is a reasonable assumption, it seems to be a quite restrictive prerequisite since there is little chance that it would be satisfied in a local area at some arbitrary time. Numerical simulations presented in previous studies have, in fact, shown that the Omori law can still emerge even if this assumption is relaxed (Ziv 2003; Ozawa & Ando 2021).

Here we investigate this issue in the case of scattered receiver faults with arbitrary initial velocity distributions. We consider the distribution of Coulomb stress changes $\Delta\sigma_f$ for receiver faults uniformly distributed around a mainshock rupture. We consider three domains with different sizes and locations encompassing a broader and a smaller area, including the entire mainshock rupture and a small area focused on the tip of the mainshock rupture (Figs 2a, d and g, respectively). Each domain is divided into 100 × 100 cells of equal size. The histograms of Coulomb stress changes are shown in Figs 2(b), (e) and (h).

We additionally consider three different distributions of initial velocities. In the first case, we use the initial velocity distribution consistent with Dieterich's assumption, that is eq. (17) (Fig. 2j, blue line). In the second case, we consider the distribution that would yield a uniform seismicity rate at no loading rate and in the absence of the mainshock perturbation. This case corresponds to the setup of our discrete fault network simulations (see Section 3). The initial velocity of Nth fault for this case is (Fig. 2j, black line)

$$V_i^N = \frac{Ar}{HN}, \tag{18}$$

Eq. (17) approaches eq. (18) as $\dot{\tau} \to 0$. Note that this initial velocity distribution would not result in an Omori decay for a uniform stress change. Finally, we consider uniform initial velocity $V = 10^{-13}$ m s^{-1} for all faults (Fig. 2j, red line). In the absence of a stress change, all faults would rupture simultaneously on day 7234 (according to eq. 15 with $A = 0.003$, $H = 48$ m, $V_i = 10^{-13}$ m s^{-1} and $\Delta\sigma_f = 0$). Therefore, the initial velocity distribution cannot explain the Omori decay in this case, and the effect of the spatial heterogeneity of the stress change is the only factor in the desynchronization of the ruptures. In this extreme case, the fact that the aftershocks follow the Omori law is only due to the stress change heterogeneity, *i.e.* the heterogeneity of stresses resulting from fault interactions since the initial stress is homogeneous.

The time to instability is calculated by randomly pairing the stress change (Figs 2b, e and h) and the initial velocity (Fig. 2j). The cumulated event count (Fig. 2k) and seismicity rate change (Figs 2c, f and i) are obtained by sorting the time to the instability of each fault. Interestingly, all three cases result in an Omori decay, including the uniform initial velocity case (Fig. 2). The Omori law appears clearer (straighter line) with a slightly higher p-value in general in the focused domain cases than in the broader domain case (Fig. 2l). The relative irregularity of the broader domain case is due to the relatively sparse sampling distance and the inclusion of the wide unperturbed area (i.e. the white area in Fig. 2a). In the broader domain case with constant velocity (Fig. 2c, red line), the seismicity rate shows a hump around day ~4000. This time is similar but slightly smaller than the time to instability without

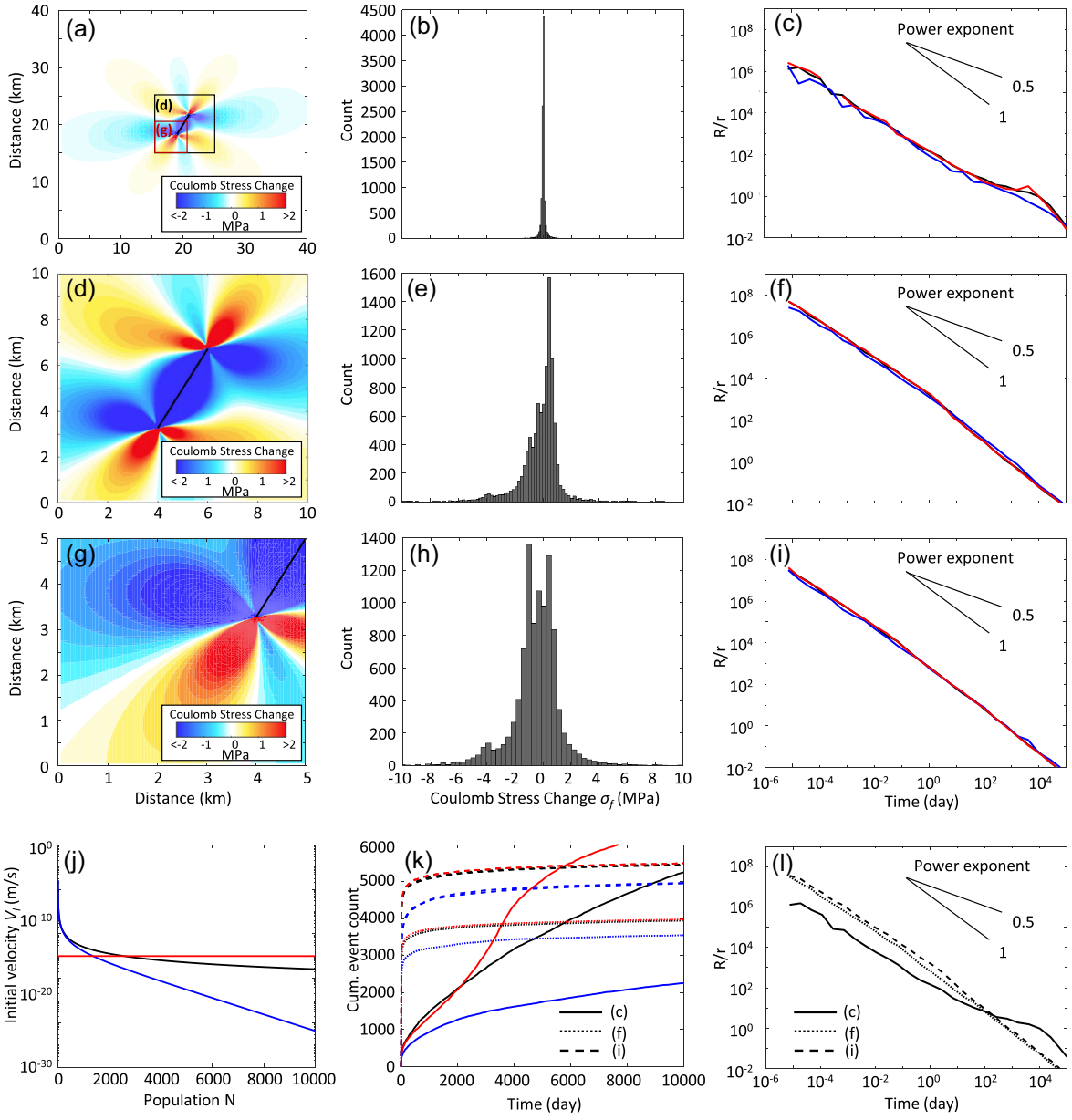

Figure 2. (a, d, g) Coulomb stress change due to 1 m of slip on a 5-km-long strike-slip fault. Receiver faults orientation is assumed parallel to the mainshock fault (black line). (b, e, h) Histograms of Coulomb stress change on receiver faults. Receivers are assumed to be uniformly distributed (100 × 100) in the domain considered (a, d, g for b, e, h, respectively). (c, f, i) Seismicity rate evolution for each domain considered (a, d, g for c, f, i, respectively). The different initial velocity distributions are represented with different colours, as defined in panel (j). (j) Initial velocity distributions (blue: eq. 17, black: eq. 18, red: uniform). (k) Cumulative event count for all cases calculated in this work (solid line: panel c, dashed line: panel f, dotted line: panel i, colours correspond to initial velocity distributions as defined in panel j). (l) Seismicity rate evolution corresponding to the black curves in panels (c), (f) and (l) (solid line: panel c, dashed line: panel f, dotted line: panel i). The values of the model parameters are the same as in our numerical simulations: $A = 0.003$, $H = 48$ m, $r = 130$ event yr^{-1} (this rate × 10 compared to our other simulations due to × 10 larger size of the fault population), and $\dot{\tau} = 500$ Pa yr^{-1}.

Coulomb stress change (day 7234). In the other cases (Figs 2f and i), the decay rate shows a better straight line with a power exponent $p = 0.8$–1, which is similar to the prediction of Dieterich's model for a non-uniform stress change (Dieterich 1994).

Clearly, the initial velocity distribution in this test does not significantly influence Omori law (Figs 2f and i). The cumulative event count shows similar curves for each stress change case regardless of initial velocity (Fig. 2k dashed and dotted lines). As noted in some previous studies (Ziv 2003; Ozawa & Ando 2021), the specific initial velocity distribution is not essential to obtain an Omori decay of aftershocks with the CRS model of earthquake triggering. The Omori law can emerge independently of the initial condition due to the heterogeneity of stress transfer, as we show here.

3. SIMULATION METHOD AND SETUP

Here, we first present the numerical simulation method (Section 3.1). The method is tested with a simple geometry for validation (Section 3.2). Simulations for more realistic fault network geometries are presented afterwards (Sections 3.3 and 3.4).

3.1 Simulation method

We consider a 2-D discrete network of faults obeying rate and state friction. The faults could have any geometry but consider only the simple case where all faults are parallel. We use a boundary element method to simulate ruptures and faults interactions. Although still idealized, the model is more realistic than the analytical model presented above as it accounts for the fact that stress transfers between faults depend on their relative locations and for the finite size of the faults system. Magnitudes are bounded by the assumed fault length distribution. We are not trying to model how the fault geometry is changing over time but rather how they interact over a period short enough that the geometry of the fault network can be considered constant.

We make a quasi-static approximation to calculate stress transfers. So, dynamic triggering is not considered, but note that it would not happen anyway with rate-and-state friction (Gomberg 2001). The fault rupture process itself is, however, simulated with account for dynamics effects, albeit with some simplification. Inertial effects are represented using radiation damping and a lumped mass approximation. The radiation damping represents wave-mediated damping dependent on slip rate (Rice 1993). The lumped mass approximation allows for inertial effects that would not be captured by radiation damping alone, such as inertial vibrations (Im & Avouac 2021). Both terms contribute to the numerical stability of the algorithm. We note that these approximations are justified as this study is primarily concerned with fault interactions and time to instability. These processes are primarily quasi-static. The most important rupture characteristic that needs to be resolved is fault slips, which control the magnitude of the stress transfer. Hence, if the final slip distribution is correctly estimated, the method used to approximate the rupture process is not critical for the purpose of this work.

Given the above approximations, the momentum balance equation at ith boundary element can be written as

$$M_i\ddot{\delta}_i = \sum_j k^{\tau}_{ij}(\delta_{0j} - \delta_j(t)) - \mu_i[\sigma'_{0i} + \sum_j k^{\sigma}_{ij}\delta_j(t)] - \frac{G}{2\beta}\dot{\delta}_i(t), \tag{19}$$

where M is the lumped mass per unit contact area for each element, δ_{0j} is the initial shear slip of element j, δ_j is the shear slip of element j from the initial slip (δ_{0j}), t is time, μ is friction, σ'_{0i} is initial effective normal stress of element i, G is shear modulus, β is shear wave speed and k_{ij} is a stiffness matrix that defines the elastic stress change imparted on element i due to slip of element j. Here k^{τ} and k^{σ} represent shear and normal stiffness matrix, respectively.

The left-hand side of eq. (19) is the lumped mass term. The lumped mass per unit area is,

$$M = \frac{\alpha\rho L}{(1-\nu)\pi^2}, \tag{20}$$

where α is a shape factor, typically close to 1, L is the average of the length and width of the fault, ρ is rock density and ν is Poisson's ratio. This term defines the equivalent mass for the inertia-dominated motion of a fault patch (Im and Avouac, 2021). On the right-hand side of eq. (19), the first term (k^{τ} term) and second term (k^{σ} term) define the shear stress and frictional stress (friction × normal stress) applied to the ith fault, respectively. The shear and normal stresses change by the displacement of a fault are calculated using the stiffness matrix k. We assume 2-D strike-slip faults so that we are in a plane-strain situation, and use the displacement discontinuity formulation (Crouch 1976) to calculate the stiffness matrix (k^{τ} and k^{σ}). The stiffness matrixes $k^{\tau}{}_{ij}$ and $k^{\sigma}{}_{ij}$ define the stress change at the centre of one fault i driven by dislocation of finite size fault j. In the simulations, except for the simple geometry test described in Section 3.2, any fault longer than 1000 m is subdivided into smaller segments. The 1000 m is much longer than the critical grid size $h^* = 2GD_c/\pi\sigma(B\text{-}A)$ (Rice 1993). This procedure is applied to allow for earthquake nucleation at any part of the large fault. Finally, the last term in eq. (19) represents radiation damping (Rice 1993).

Our method does not resolve the process zone near the tip area (e.g. Scholz *et al.* 1993). As a result, the stress change can be infinite near the fault tip, whereas in reality, it would be bounded by the finite strength of the medium. Furthermore, fault distribution is random, so the fault density can be unreasonably high. Hence, irrealistic strong fault interactions can result if they are too close, which results in numerical instability. We applied 'too-close' criteria at $k^{\tau}{}_{ij}/k^{\tau}{}_{ii} > 0.8$ and $k^{\sigma}{}_{ij}/k^{\tau}{}_{ii} > 0.8$. If either one of the criteria is satisfied, the element of a shorter fault is removed from the simulation.

Eq. (19) is solved with rate and state friction law eqs (1), (2) or (3). When fault slip velocity is high, it is solved with the method of Im *et al.* (2017, 2021), which shows good numerical stability during the rupture process. The increased stability allows multiple simulations with randomized fault geometry with various complexity. The time step is adopted based on the highest slip velocity but automatically reduced when there is no convergence.

3.2. A test case with a simple set of faults

Our modelling method is illustrated with a simple four-fault system (Fig. 3), including a central main fault (black line) surrounded by smaller faults (red, blue, and green lines). In the simulation, the main fault (black) is close to rupturing with an initial velocity of 10^{-7} m s^{-1}, whereas other faults are further away from rupturing with an initial velocity of 10^{-10} m s^{-1}. The responses of the small faults are compared with the shear, normal, and Coulomb stress change calculated by the central black fault rupture displacement with displacement discontinuity formulation (contour of Figs 3a, c and e).

The simulations represent well the spatial correlation between the aftershock location and Coulomb stress change in nature (King *et al.* 1994; Harris 1998). The mainshock (black) ruptured at ∼490 s, and the other smaller faults responded to the stress change driven by the mainshock. Two of the small faults (blue and green) are located in the area of Coulomb stress increase (Fig. 3a). The simulation results show that the slip velocities of those faults are significantly increased as a result of the main fault rupture (Fig. 3b). The velocity increase is larger for the blue fault, which is located in a lobe of a larger Coulomb stress increase than the green fault. The blue fault ruptures almost simultaneously with the mainshock, whereas the green fault ruptures after ∼150 s from the mainshock. These two ruptures are aftershocks. The velocity of the red fault, which is located in a lobe of negative Coulomb stress change, strongly declines during the mainshock rupture and the rupture is therefore delayed as expected.

Static stress changes correspond to the simulation design, that is the stress calculated from the displacement discontinuity method (Crouch 1976; Figs 3c–f). For example, the estimated shear stress change for the red and green fault by the mainshock is ∼−0.3 and ∼+0.1 MPa, respectively (Fig. 3c contour), which corresponds well to the simulation result (Fig. 3d). The shear stress of the blue fault rapidly increases during the mainshock and then drops abruptly due to the rupture of the fault (Fig. 3d). The normal stress change for

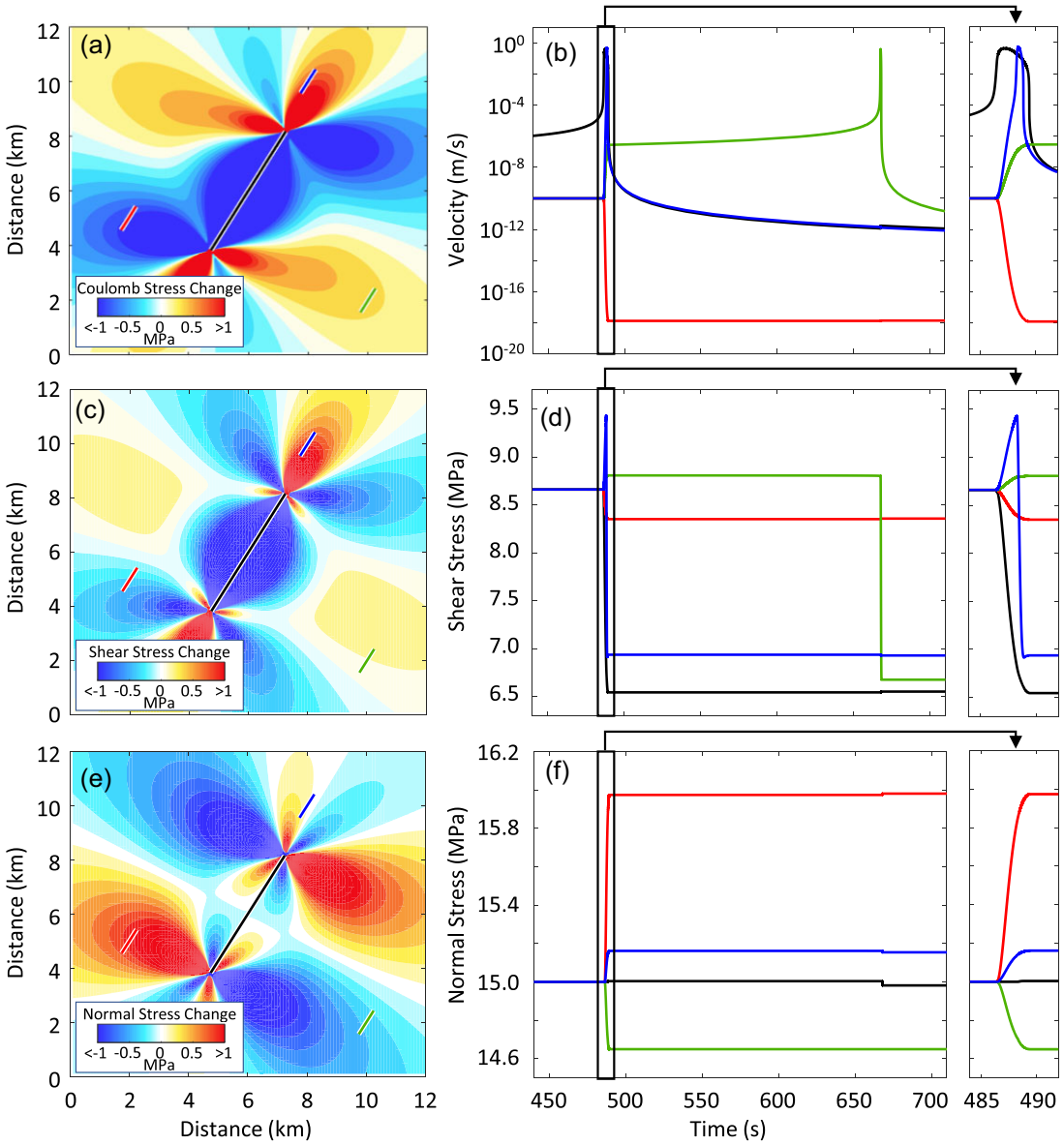

Figure 3. Simulation results with four discrete faults. The 5-km-long main fault (black line) is located at the centre and is close to rupturing (initial velocity of 10^{-7} m s^{-1}). The other three 1-km-long faults are far from rupturing (initial velocity 10^{-10} m s^{-1}). (a, c, e): Contour maps represent the Coulomb stress (a), shear (c) and normal stress change due to 0.67 m shear slip of the main fault calculated by the displacement discontinuity method (Crouch 1976). The value of 0.67 m is the slip predicted by the simulated rupture of the main fault. (b, d, f): Predicted velocity (b), shear stress (d), and normal stress (f). The colour coding refers to the 4 faults in all panels. Simulation is conducted with ageing law (see slip law for Supporting Information).

the red, green, and blue faults are ∼+1, ∼−0.4 and ∼+0.2MPa, respectively (Fig. 3e contour). This result also corresponds well with the simulation result (Fig. 3f). The simulation result shows small stress perturbation at ∼660 s driven by green fault rupture (e.g. normal stress change on the blue and black faults at ∼660 s in Fig. 3f), indicating that all faults interact with each other with the moment-dependent interaction magnitude.

We conducted an extra simulation with the slip evolution law (Fig. S1). The results are qualitatively similar to those obtained with the ageing law (Fig. 3), but the nucleation process is faster (black fault ruptured at 30 s). Accordingly, aftershocks rupture (green fault) sooner after the mainshock.

3.3. Main simulation setup—the main fault embedded in a complex fault zone

We conducted 100 simulations with a complex fault zone geometry. We assumed a 100 m wide and 10-km-long fault zone consisting of multiple faults with various lengths (Figs 4a inset and 5a red fault area). The fault zone is surrounded by an ‘off-fault’ area containing randomly distributed smaller faults (Fig. 5a blue and grey faults). The length of individual fault is randomly selected between 50 and 5000 m in the fault zone and between 50 and 3000 m outside of it. A self-similar fault length distribution (Fig. 4b) is adopted to yield

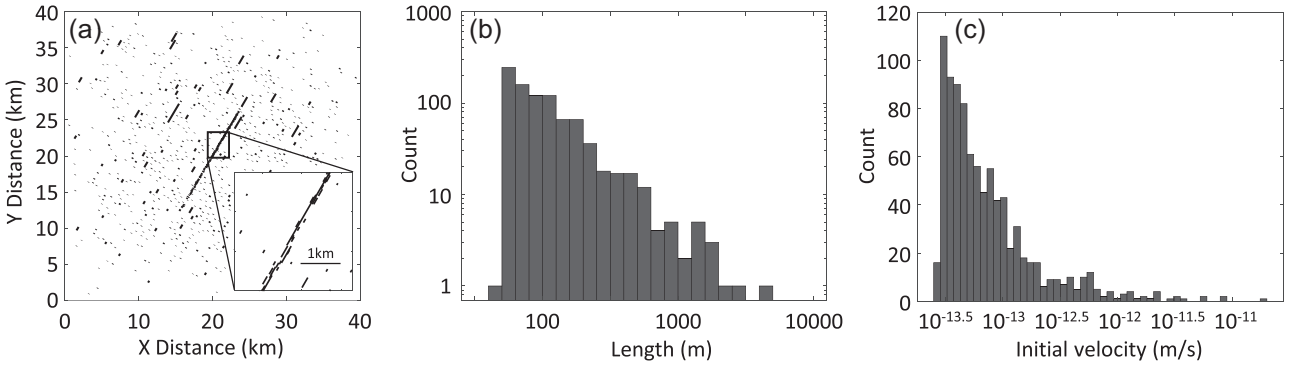

Figure 4. Distribution of fault locations, length and initial velocity of the reference simulation. (a) Spatial distribution of fault. Each line represents a single fault. About 20km-long mainshock fault zone (centre) consists of multiple smaller faults (inset). (b) Fault length distribution. The set was drawn randomly from a probability density function to yield the Gutenberg–Richter distribution (Fig. 6b). (c) Distribution of initial velocity. The initial velocity distribution is selected to yield a constant seismicity rate.

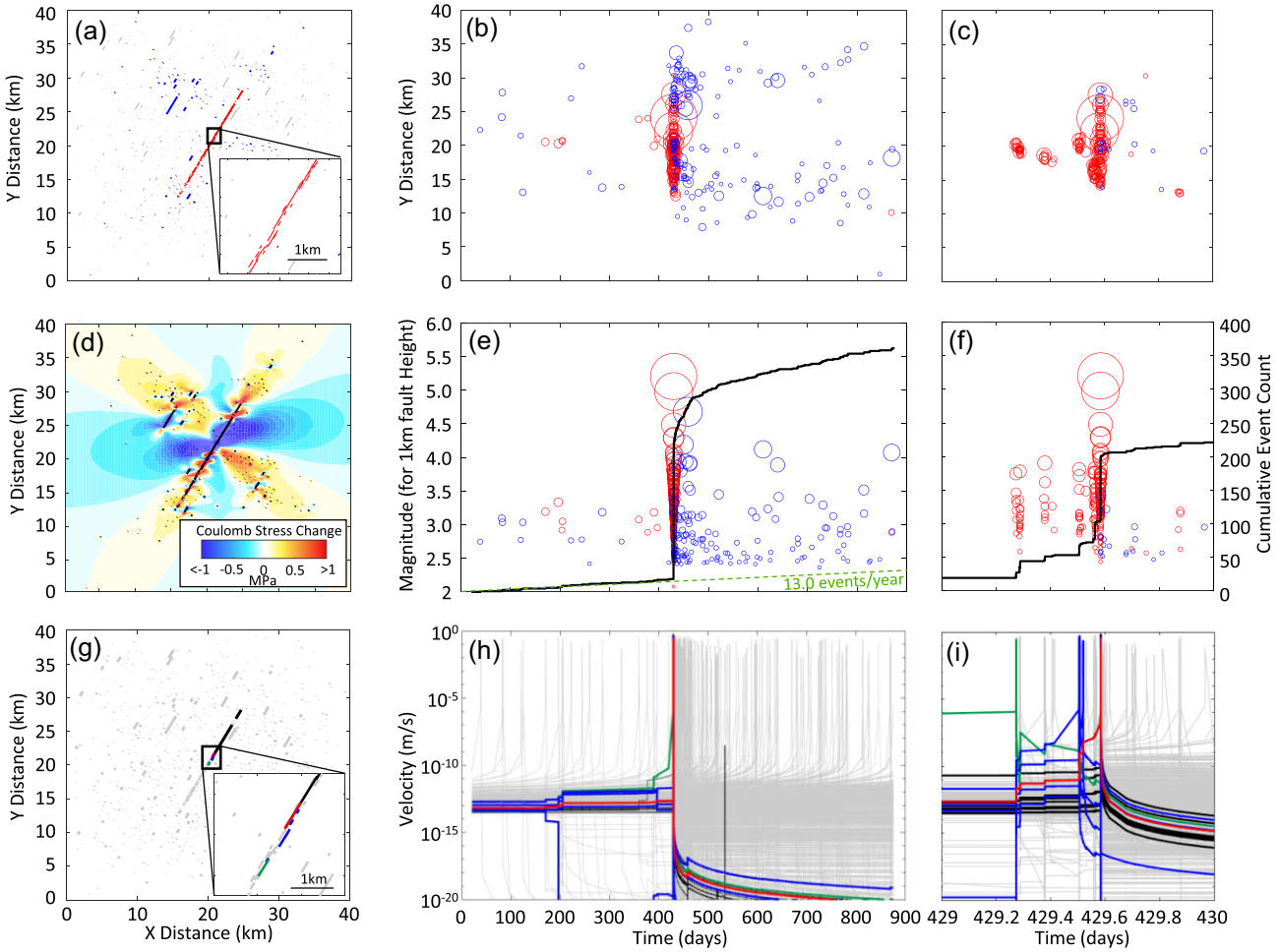

Figure 5. Reference simulation result. (a) The coloured (red and blue) faults are ruptured during the simulation, whereas the grey faults are not. Red and blue colours represent fault-zone and off-fault-zone ruptures, respectively. (b, c) Location versus time for the whole duration (b) and the day of the mainshock (c). Colours correspond to (a). (d) Coulomb stress change (contour) at the end of the simulation with ruptured faults (black lines). (e, f) Event magnitude versus time for the whole duration (b) and the day of the mainshock (c). The bold black line denotes the cumulative event count. The green dashed line in (e) denotes the theoretical seismicity rate with no faults interaction. Colours correspond to (a). (g, h, i) Fault slip evolution for the mainshock (red, black) and a selection of foreshocks (blue, green) and other faults (grey). The mainshock nucleated on the red segment of the main fault. (h, i) Velocity versus time for the whole duration (h) and the mainshock day (i). The key faults for the foreshock sequence are coloured. The colours correspond to (g). Some angularness of the curves in (i) is due to the sampling rate (see Fig. S2 for slip law result).

the Gutenberg–Richter law. If a fault length is longer than 1000 m, it is subdivided into smaller segments with a length smaller than 1000 m. With this segmentation, the nucleation can occur on any subsegment of a long main fault. Selecting a lower threshold would be possible but would increase the computational cost. We found that the choice of a 1000 m element size is a reasonable compromise.

Initially, 200 fault-zone faults and 800 off-fault-zone faults are generated. All faults are strike-slip faults with a 30° angle from the north to the east. After applying the 'too-close' criterion, average 141 fault-zone faults remain. This criterion filters out faults mostly in the fault zone due to the high density of faults there.

The initial velocity of each fault is randomly selected within the distribution that would generate a constant seismicity rate. All faults in this simulation are initially well-above-steady-state (i.e. $\theta_i >> D_c/V_i$). Given that our simulation does not account for tectonic loading, the time to instability is according to eq. (16) with $\Delta\sigma_f = 0$,

$$t = \frac{A}{HV_i}, \tag{21}$$

where A is a rate and state friction parameter and V_i is the initial velocity of the fault. The time to failure is then inversely proportional to the initial velocity ($1/V_i$). To impose constant seismicity, we randomly select the inverse of initial velocity ($1/V_i$) between 0 and 3.5 $\times$ 10^{13} s m^{-1}. Considering the simulation parameters, $A = 0.003$ and average $H = 48$ m (average $k^r{}_{ii} \sim 1.8 \times 10^8$, initial normal stress $\sigma = 15$ mPa, $B = 0.006$ and $D_c = 100$ μm s^{-1}), $(1/V_i) = 3.5 \times 10^{13}$ s m^{-1} (i.e. $V_i \sim 10^{-13.5}$ m s^{-1}) yields time to instability $t = 2.19 \times 10^9$ s, which is the expected maximum. Since our reference simulation contains 900 faults that yield random rupture up to $t = 2.19 \times 10^9$ s, the average inter-event time is 2.43×10^6 s, yielding an expected yearly seismicity rate of ∼13.0 events yr^{-1}.

We recall that the simulations presented so far do not consider the tectonic loading rate. The faults are, however, assumed to be loaded by regional tectonics, but the resulting stresses are assumed constant over the simulation period. The assumption is that the stress changes from faults interaction are large compared to the stress change due to tectonic loading over the time we analyse here. To verify this assumption, we additionally conducted 100 simulations with a tectonic loading rate which is presented in the Supporting Information (Figs S3 and S4). In the simulations, initial velocities are randomly set based on eq. (17) (instead of eq. 18) with a tectonic loading rate of 10 kPa yr^{-1}, which corresponds to the estimated interseismic loading rate of the San Andreas fault (Freed *et al.* 2007). The behaviour observed in that simulation is not different from the behaviour observed in the simulations with no tectonic loading rate.

3.4. Extra simulations—investigation of foreshock and aftershock mechanism

To investigate the characteristics of foreshock and aftershock sequences generated with this model, we conducted 250 additional simulations with different settings. First, we conducted simulations with varied fault zone complexity. In addition to the main simulation with a complex fault zone with 200 faults (Fig. 4), we conducted 4 sets of 50 simulations with 1, 50, 100 and 150 faults in the fault zone. The total number of faults is initially 1000 in all simulations. For example, for the 1 fault count case, all 1000 faults are randomly distributed in the simulation domain, except only one long mainshock fault is kept at the centre of the domain. Increasing fault-zone fault count represents increasing fault zone complexity. Since the magnitude of the interaction between the faults (ΔS in eq. 5) is dictated by fault density, this set of simulations allows us to investigate how foreshock acceleration changes with the interaction stress ΔS.

We also conducted 50 simulations with uniform initial velocity (10^{-13} m s^{-1}) for all faults except one segment of the mainshock fault with a higher initial velocity (10^{-7} m s^{-1}). In this setup, the mainshock ruptures almost immediately after the beginning of the simulation. All the other faults will respond to the stress change from the mainshock. Since we set a uniform initial velocity for the aftershock fault, this simulation completely removes the initial velocity effect on the aftershock sequence. In this test, we essentially reproduce the uniform velocity case in Section 2.3 (red curves in Fig. 2).

4. SIMULATION RESULTS

We show here that the simulations yield realistic earthquake catalogues, including swarms and occasional foreshock and aftershock sequences (Section 4.1). All simulation shows clear aftershock sequences with an Omori law decay. Foreshocks are only apparent when the fault zone is complex and dense enough; the foreshock sequence disappears when the complexity is removed (Section 4.2). The Omori law is still observed even when the faults have a uniform initial velocity (Section 4.3).

4.1 Main simulations—main fault embedded in a complex fault zone.

The simulations are conducted 100 times with randomly generated fault length, fault location and initial velocity within the forementioned probability density. The simulations include a dense fault zone, where strong interaction is expected. We select one simulation as a reference simulation and investigate the result in detail (Section 4.1.1). Then three more simulations with distinct sequences are briefly discussed (Section 4.1.2). Finally, we discuss stacked foreshock and aftershock sequences (Section 4.1.3).

4.1.1 Detailed result of a selected reference simulation

Among the 100 simulations we conducted, we selected one reference simulation to investigate how foreshock and aftershock sequences evolve in detail (Fig. 5). The reference simulation extends over ∼900 d. The mainshock (major rupture of the central fault zone) ruptured on day 429 (Fig. 5e). Before the rupture, the seismicity rate was roughly consistent with the expected rate, given the initial velocity distribution, of ∼13 events yr^{-1} (green dashed line in Fig. 5e). Once the mainshock occurs, the seismicity rate significantly increases (Fig. 5e). The seismicity rate then gradually decreases with time, as observed during aftershock sequences in nature (Utsu *et al.* 1995).

Aftershocks result from the time advance process illustrated by our simplified four-fault simulation (Fig. 3). The mainshock strongly influences the slip velocities of most faults. Once the mainshock ruptures, the velocities of the other faults are significantly perturbed. The velocity distribution becomes much wider after the mainshock (after day 430 of Fig. 5h velocity distribution of grey faults becomes significantly thicker). As observed in our simplified simulation in Fig. 3, this is due to the stress change from the mainshock. Once the mainshock occurs, Coulomb stress in the domain is significantly changed (Fig. 5d). If a fault is located in an area of Coulomb stress increases due to the mainshock, its velocity is increased, and the time to instability is reduced. These

triggered fault ruptures are direct aftershocks, as theoretically predicted by Dieterich (1994). Aftershocks also occur in the stress shadows of the main rupture. They are the result of secondary aftershocks (aftershocks of previous aftershocks) and are, therefore, a clear manifestation of the cascading process (Marsan 2005; Meier *et al.* 2014).

The temporal evolution of aftershock rate follows a power-law decay (Fig. 6) consistent with the modified Omori law (Omori 1894; Utsu *et al.* 1995),

$$n(t) = \frac{K}{(t+c)^p}, \tag{22}$$

where K, c and p are constant. The modified Omori law defines aftershock rate (n) decay with power-law with power exponent p. The p-value of ∼0.8 (Fig. 6a) is well within the range of typical p-values observed in nature. For example, in California, the average p-value is ∼1.07 and is distributed within the 0.5∼1.5 range (Reasenberg & Jones 1989). Our synthetic earthquake catalogue also follows the Gutenberg–Richter law with a b-value close to 1 (Fig. 6b). This result is due to the model design given the choice of the fault length distribution (Fig. 4b). The results are very similar whether the ageing or slip law is used.

A zoom-in view of the mainshock day (Figs 5c, f and i) reveals three clusters in the few hours before the mainshock. These foreshocks are located near the epicentre. In the simulation, the mainshock rupture (black fault in Fig. 5g) nucleated on the red segment (Fig. 5g inset). The rupture of the red segment is advanced by several foreshocks (blue and green in Figs 5g, h and i). Figs 5(h) and (i) shows the velocity history of the mainshock fault and the triggering events. The initial velocity of the red segment of the mainshock fault was $\sim 10^{-13}$ m s^{-1} (Fig. 5h, red line). If the fault were isolated and unperturbed, according to eq. (16), the mainshock would have occurred on day ∼7000. It is clear that the foreshocks have all accelerated the slip rate on the main fault and therefore contributed to advancing the mainshock rupture at day 429.

The red segment of the main fault experienced several step-velocity-increases before the rupture (Fig. 5i). The most significant velocity change (i.e. direct triggering of the mainshock) corresponds to the clustered rupture of blue faults about 0.1 d before the mainshock. These clustered events increased the velocity of the mainshock (red) from 10^{-11} to 10^{-8} m s^{-1} (red line stepping at ∼429.5 d in Fig. 5i). These blue faults, on the other hand, were advanced at day ∼429.3 by the green fault (Fig. 5i), which also advanced the mainshock rupture. The cascading is thus not a simple process of pairwise causal interactions. The rupture time of a fault is affected by all previous nearby events and, in turn, influences the subsequent rupture time on nearby faults.

The triggering chain started, in fact, at a much earlier time. Fig. 5(h) shows that the green fault was already strongly stimulated ∼50 d before the mainshock. This stimulation is due to a rupture in the fault zone. Without this stimulation at day ∼390, the green fault would have ruptured much later, and accordingly, the mainshock would have happened later as well. There are even earlier foreshocks at day ∼200. This early foreshock stimulates blue and green faults ∼230 d before the rupture (Fig. 5h).

Although the inverse Omori law acceleration of seismicity rate is not apparent in single sequences of foreshocks, the simulation demonstrates that foreshocks become statistically more frequent closer to the rupture time of the mainshock. Our analytic expression in Section 2.2 predicts this behaviour. In Section 4.2, we check that the inverse Omori law becomes apparent when simulations are stacked, as is the case when natural sequences are stacked (Jones & Molnar 1979; Bouchon *et al.* 2013).

4.1.2 Distinct sequences of three selected case

We further selected three different simulations that show distinct foreshock and aftershock sequences. In the first case (Figs 7a and b), a significant foreshock swarm occurs about 30 d before the mainshock. This foreshock swarm shows clear migration patterns. It migrates towards both $+y$ and $-y$ directions. The migration towards the $+y$ direction stops within a few days (Fig. 7a, right-hand panel), and the migration towards $-y$ direction seems to last for a much longer duration (Fig. 7a). The mainshock rupture occurs about 30 d after the foreshock swarm. The epicentre is located near the area where $+y$ migration is arrested.

The second case shows no dominant mainshock (Figs 7c and d). Instead, the central fault zone is ruptured in three separated clusters of smaller events ($M \sim 4$). The three clustered events clearly migrate towards $-y$ direction (Fig. 7c, right-hand panel) in ∼5-d intervals. An early foreshock at day ∼300 is also observed in Fig. 7(c). Interestingly, the aftershock sequence appears to be insignificant. The seismicity rate rapidly returns to the original rate (13 events yr^{-1}) within less than 100 d. These behaviours are presumably driven by the fault geometry. The fault zone likely consists of ill-connected short faults. Hence, a large rupture could not be developed, and accordingly, the aftershock sequence is insignificant. This simulation demonstrates that swarm-like migrating clusters can result from cascading alone in a Discrete Fault Network model, as it can happen in ETAS simulations as well (Helmstetter & Sornette 2002).

In the third case, the seismicity rate accelerates starting a few hundred days before the mainshock rupture (Fig. 7f). A similar acceleration of the rate of foreshocks is often observed in stacked sequences but is generally not apparent in a single foreshock sequence (Helmstetter *et al.* 2003; Bouchon *et al.* 2013; also see Section 3.3). However, this specific case demonstrates gradual acceleration well before the mainshock rupture. Interestingly, the foreshock sequence stops a few days before the mainshock, and the mainshock rupture does not have an immediate foreshock in the last few days (Figs 7e and f, right-hand panel).

4.1.3 Stacked simulation results

Out of the 100 simulations conducted, we stacked 67 simulation results, which have mainshock occurred at least 500 d after the beginning of the simulation (Fig. 8a). Most of the individual foreshock sequences (Fig. 8a grey and black lines) are strongly clustered without showing a gradual accelerating foreshock rate. However, once stacked, gradual acceleration of the foreshock sequence is apparent (Fig. 8a, red line). The stacked foreshock rate is higher than the background rate, even as early as 500 d before the mainshock (Fig. 8, green dashed line).

The stacked simulations follow the Omori law (eq. 21) and the inverse Omori law, $n(t) = K'/(t_c - t)^{p'}$ for a p-value of the order of 0.8 (Fig. 8b), as seen in the reference simulation. The power-law exponent for the foreshocks appears to be similar to or slightly smaller than for the aftershocks (Fig. 8b). The initial plateau of seismicity rate at time $t < c$ (eq. 22) is not visible though, implying a value of less than a few minutes, which is under the resolution of our simulation due to the sparse sampling rate (1 per 500 time step) that we apply to limit the data size. The low c-value in this simulation is consistent with the view of Kagan & Houston (2005)

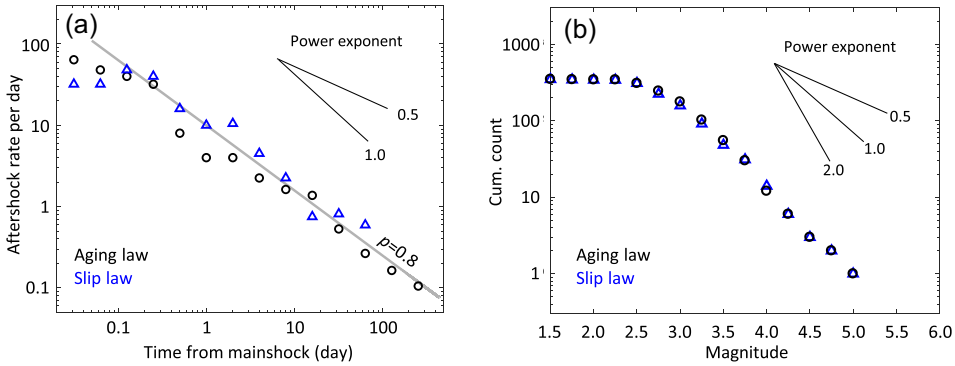

Figure 6. Omori law and Gutenberg–Richter law of the reference simulation result. Black circles and blue triangles show results obtained with the ageing (Fig. 5) and slip law, respectively (Fig. S2). (a) Aftershock rate with time in log-log scale. The grey line is the reference line for power exponent $p = 0.8$. Other reference power exponent slops are shown in the upper right area. (b) frequency–magnitude distribution. The plots show the cumulated number of events with magnitudes above the value in abscissa. The simulation follows well the Gutenberg–Richter law, with a *b*-value close to 1.0, as intended by choice of the fault length distribution (Fig. 4b).

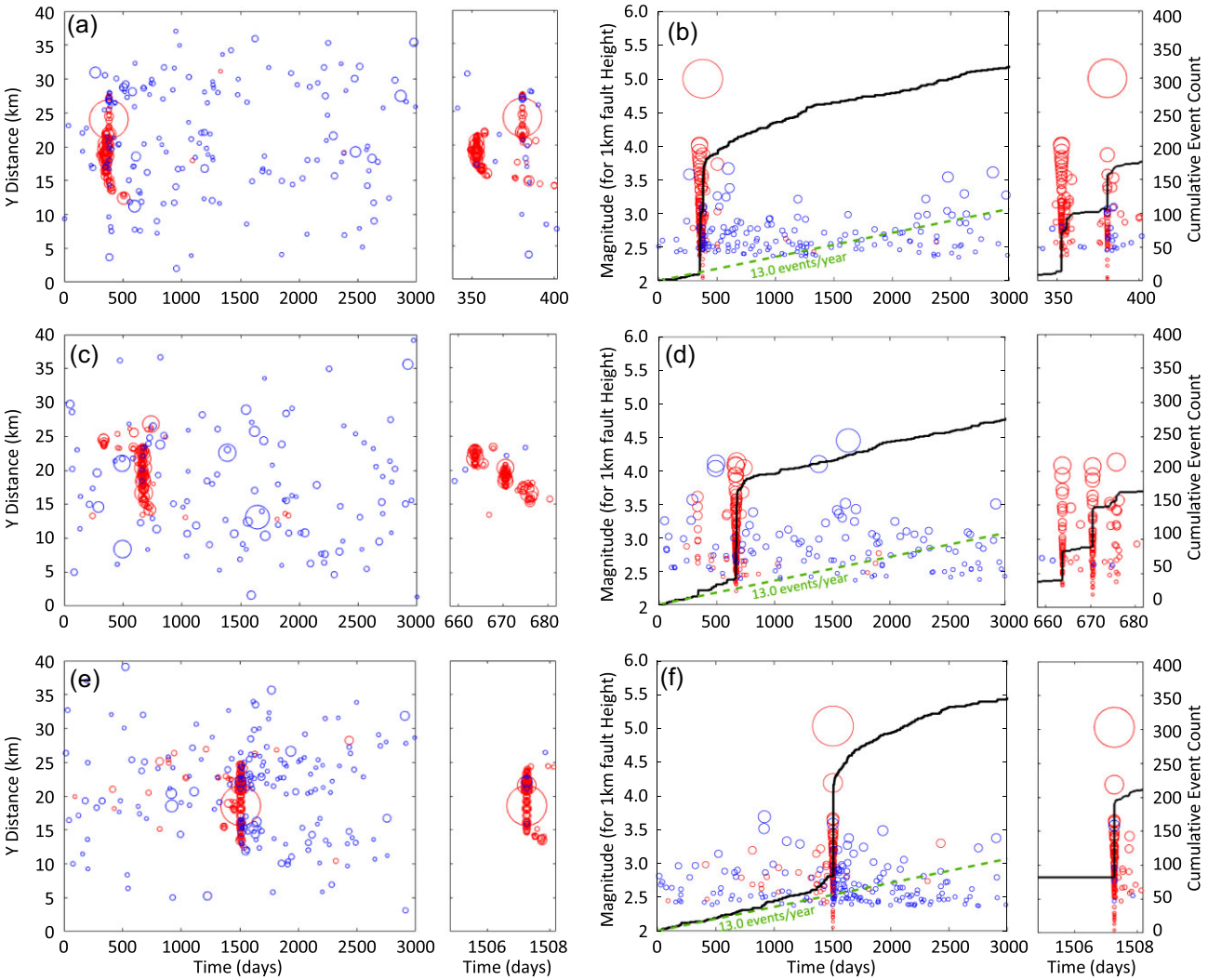

Figure 7. Three selected examples of distinct foreshock and aftershock sequences. Red circles denote seismic events within the mainshock fault zone, and blue circles denote the events outside the fault zone. (a, b) A case with a single large foreshock swarm about 30 d before the mainshock. (c, d) A case with migrating clusters. (e, f) A case with accelerating foreshocks.

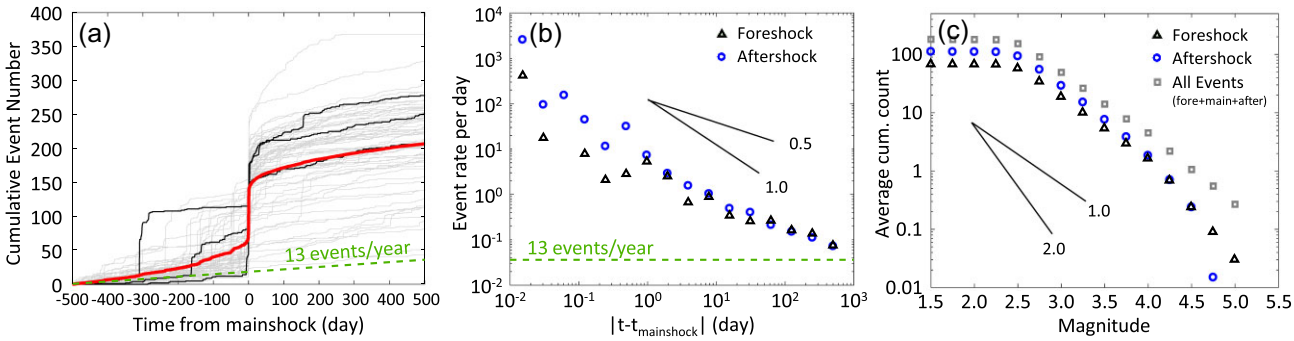

Figure 8. (a) Cumulative seismicity with time before and after the mainshock. Grey lines denote 67 simulation results that have mainshock occurring after 500 d. A few cases are highlighted in the black line. The bold red line denotes the stacked average. (b) Event rate versus time form mainshock for both foreshock (black triangle) and aftershock (blue circles). The green dashed line denotes the seismicity rate in the case of no cascading interaction. (c) Average cumulative event versus magnitude plot of the events shown in panel (a). Black triangle denotes foreshock, blue circles denote aftershock and grey square denotes all events, including the mainshock.

that the c-value is likely very low in nature as well, possibly as low as 5 min (Enescu *et al.* 2007). We note, however, that the detection of c in real catalogues is difficult due to coda-waves which can obscure the detection of aftershocks early after the mainshock (Enescu *et al.* 2007; Kilb *et al.* 2007).

Stacked simulations also follow the Gutenberg–Richter law (Fig. 8c). In general, all events shown in Fig. 8(c) show a linear trend in the log-log scale with a power exponent (the b-value) of ∼1.0 (Fig. 8c grey square). This result is not surprising, given the fractal length distribution (Fig. 4b). The foreshock and aftershock trends both show some tapering at large magnitude due to the removal of the mainshock (in Fig. 8c). The tapering appears stronger in the aftershock sequence than in the foreshock sequence. This relative abundance of large-magnitude events in the foreshock is also implied in Fig. 8(a). Strongly clustered events (the step increases of the grey line) are more frequently observed in the foreshock sequence than in the aftershock (Fig. 8a, grey lines). The Gutenberg–Richter b value is also slightly larger in the aftershock sequence than in the foreshock. This simulation result is reminiscent of the observation that the b value seems smaller for foreshocks than for aftershocks (Gulia & Wiemer 2019).

4.2 Fault-zone complexity and foreshock

We hypothesized, in Section 2, that the foreshock result from fault interactions (ΔS in eq. 5), which are controlled by the density of the fault distribution. In this view, the high density in the fault zone in the simulations with a complex fault zone (Fig. 4a, inset) is likely the cause of the observed accelerating sequences of foreshocks. To confirm and quantify this effect, we conducted 4 sets of 50 additional simulations with varied fault zone complexity represented by fault zone fault count 1, 50, 100 and 150. In practice, we vary the number of faults within the fault zone. The final counts of faults within the fault zone after application of the 'too close' criterion for the four sets are, on average, 1 (for 1 initially), 42 (for 50 initially), 78 (for 100 initially) and 108 (for 150 initially), in addition to our complex fault simulation in the previous section 141 (for 200 initially).

The simulation result shows no detectable foreshock acceleration when fault zone complexity is removed (1 fault-zone fault case; Figs 9a and b), indicating that the foreshock acceleration in the reference simulation (Fig. 8) indeed results from the dense fault distribution in the fault zone. The average seismicity before the mainshock remains roughly at the expected seismicity rate (13 events yr^{-1}, Fig. 9b) all the way until the mainshock. The simulation result fits the expectation from our foreshock mechanism, indicating that the magnitude of stress interaction controls the foreshock acceleration.

In the case of weak interaction, aftershock still follows Omori law decay (Fig. 9b), but the decay rate seems to be smaller than in the case of a dense fault zone (compare the slope between Figs 9b and 8b), especially for the short-term ($t - t_m < 1$ d). This is due to the removal of dense fault distribution of the fault zone. The fault zone faults are located in the high Coulomb stress increase area (Fig. 5d) and, accordingly, respond immediately to the mainshock. In the no-fault-zone simulations, those immediately responding faults are removed, and therefore the aftershock decay rate is reduced, particularly at the early time. This observation shows that the Omori exponent p is also dependent on the spatial distribution of critically stressed fault.

The simulations with varied fault zone density further show that the foreshock acceleration is systematically dependent on the complexity of the fault zone (Fig. 10). The inverse Omori law exponent increases with the complexity of faults from 0 to ∼0.6 (Fig. 10e). Those power exponents are smaller than our analytically driven inverse Omori law exponent 1 (Fig. 1), presumably due to the mean-field approximation providing an incomplete quantification of the distribution of stress interactions. Nevertheless, our simulations demonstrate well that the foreshock acceleration is dictated by faults interactions within the fault zone hosting the mainshock.

4.3 Uniform initial velocity case

Our reference set of simulations (Fig. 8) shows an apparent Omori decay during aftershock sequences. Although we adopted some of the assumptions that Dieterich (1994) used to derive his aftershock model (sources well-above-steady-state and the principle of the time to instability calculation), there is a material difference. We imposed initial velocities to get a constant seismicity rate at zero loading rate (eq. 21). By contrast, the Dieterich model assumes initial velocities to get constant seismicity with a non-zero loading rate. We have seen in Section 2.3 that the initial velocity distribution is actually not essential to obtain an Omori decay during aftershock sequences and argues that the influence of the initial velocities is overprinted by the heterogeneous stress changes imparted by the sequence of earthquakes.

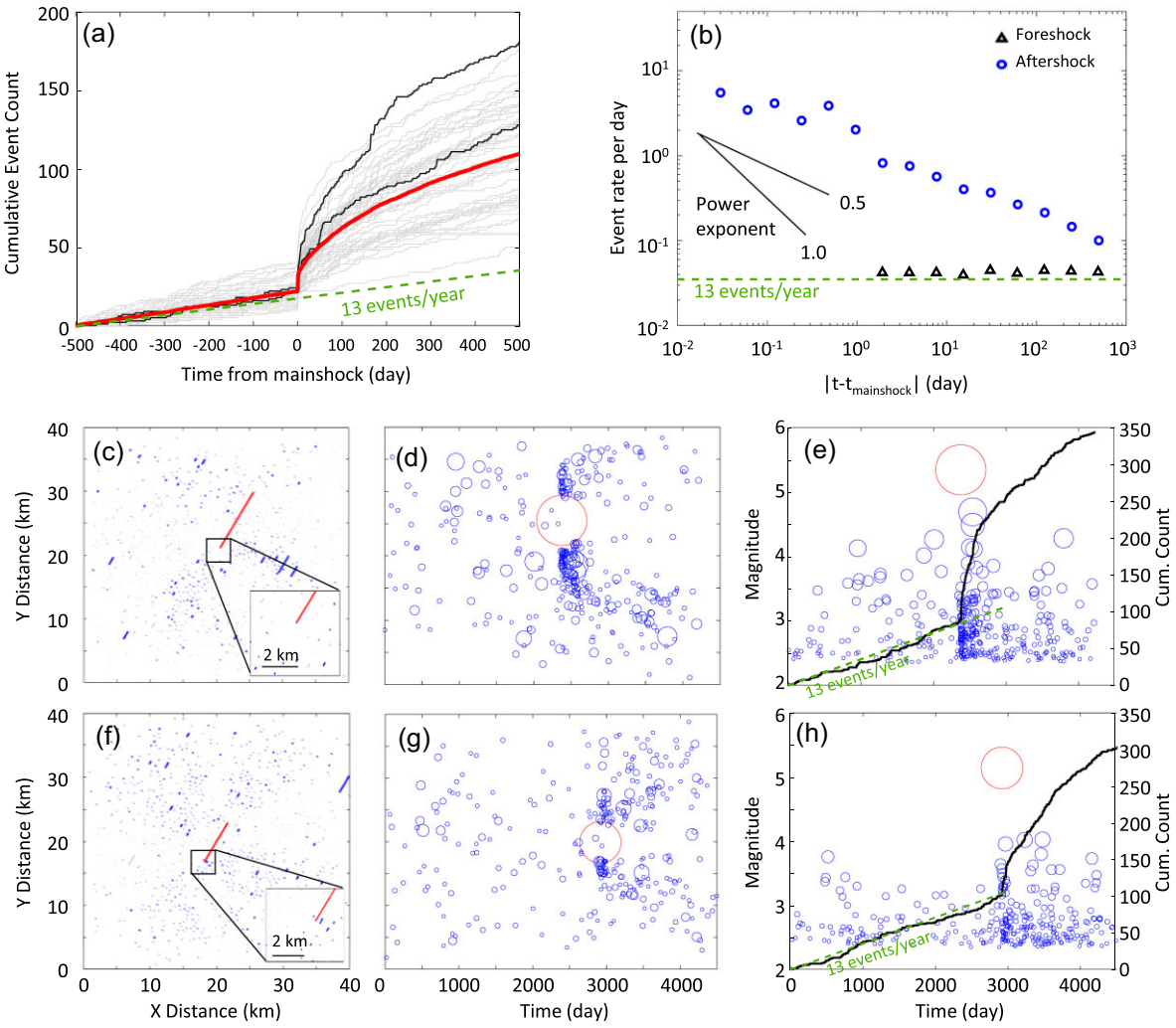

Figure 9. Simulation results in the case of weak fault interaction. The model setup does not include any complex fault zone. (a) Cumulative seismicity with time before and after the mainshock. The red line shows the fault ruptured in the mainshock, which consists of a simple linear segment with no secondary faults nearby. Grey lines show all 50 simulation results. Two selected cases (panels e and h) are highlighted as black lines. The bold red line is the stacked average. (b) Event rate versus time from mainshock for both foreshocks (black triangle) and aftershocks (blue circles). The green dashed line corresponds to the seismicity rate expected in the absence of interaction (no cascading). (c–h) Simulation results for the two selected cases. (c, f) Fault network geometry. The faults ruptured during the simulation are shown in colour (red for the mainshock and blue for the others). The grey faults are not ruptured. The fault zone consists of only one large fault (inset). (d, g) Event location (projected on *Y*-axis) versus time for all events. (e, h) Event magnitude and cumulative count for all events.

We have verified this hypothesis using our discrete fault network. We conducted 50 simulations with uniform initial velocity to all the faults except the main fault. We use the same fault network with a no-fault-zone as the one presented in Fig. 9. We make sure that the mainshock rupture happens early in the simulation by assigning a high initial velocity (10^{-7} m s^{-1}) to one segment of the mainshock. All the other faults have uniform low initial velocities (10^{-13} m s^{-1}). They would all rupture at day ∼7000 in the absence of the mainshock. We observed that each fault is sent on a new path to rupture at the time of the mainshock so that the faults are quickly not synchronized anymore. As a result, the Omori decay is still observed (Fig. 11). The power exponent of the stacked aftershock sequence is lower than in our reference model (∼0.5 Fig. 11b) and close to that expected for the large domain case (Fig. 2c). The rupture time of individual faults is primarily dictated by the magnitude of Coulomb stress change (eq. 15), which decreases with distance from the mainshock. This effect results in a notable aftershock migration pattern (Fig. 11d).

5. COMPARISON TO ETAS MODEL

The swarm, foreshock and aftershock sequences observed in our numerical simulations can, in principle, be observed in ETAS simulations (Helmstetter & Sornette 2002). We, therefore, compare the two types of simulation in this section. Our discrete fault network simulations and ETAS simulations are both producing earthquake cascades, but there are essential differences: (i) our model is physics-based, whereas ETAS is statistics-based; (ii) in our model, any earthquake is influenced by the stress transfers from all previous events whereas in ETAS, earthquake is triggered by only one 'mother' earthquake; (iii) the Omori law is explicitly embedded in the ETAS formulation, whereas, in our model, it naturally results from stress transfers and the earthquake nucleation process and (iv) in our model, clusters results from the time-advance of ruptures on a pre-existing network of faults, whereas ETAS assumes an additive process. In this section, we show how these differences play.

The ETAS model (Kagan & Knopoff 1981; Ogata 1988, 1998) is a statistical model designed to accommodate the empirical Omori

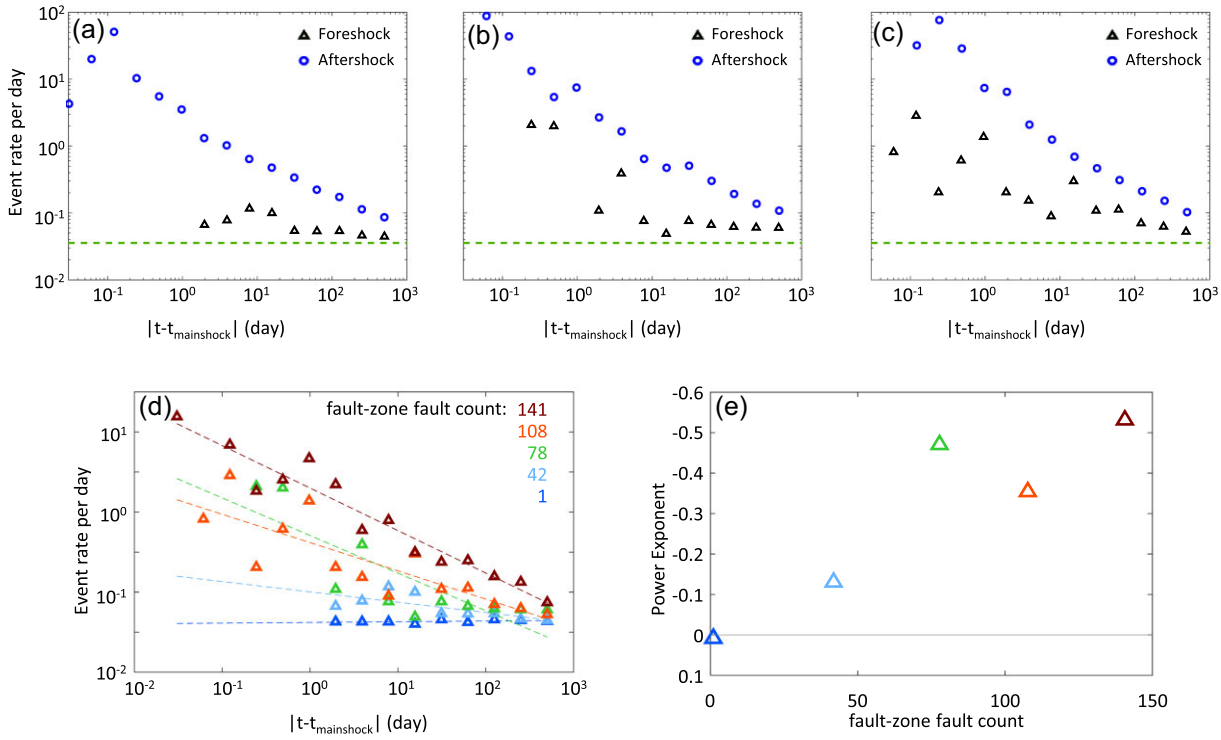

Figure 10. Simulation results with varied fault interaction. (a–c) The stacked foreshock and aftershock rate versus time relative to the mainshock occurrence time for the fault zone fault counts of ∼42 (for 50 initially), ∼78 (for 100 initially) and ∼108 (for 150 initially). See Fig. S5 for the cumulative event count. The foreshock results in (a)–(c) and the previous simulations (Figs 8c and 9b) are plotted together in panel (d) with power-law fit. (e) The power exponents of the power-law fit in panel (d).

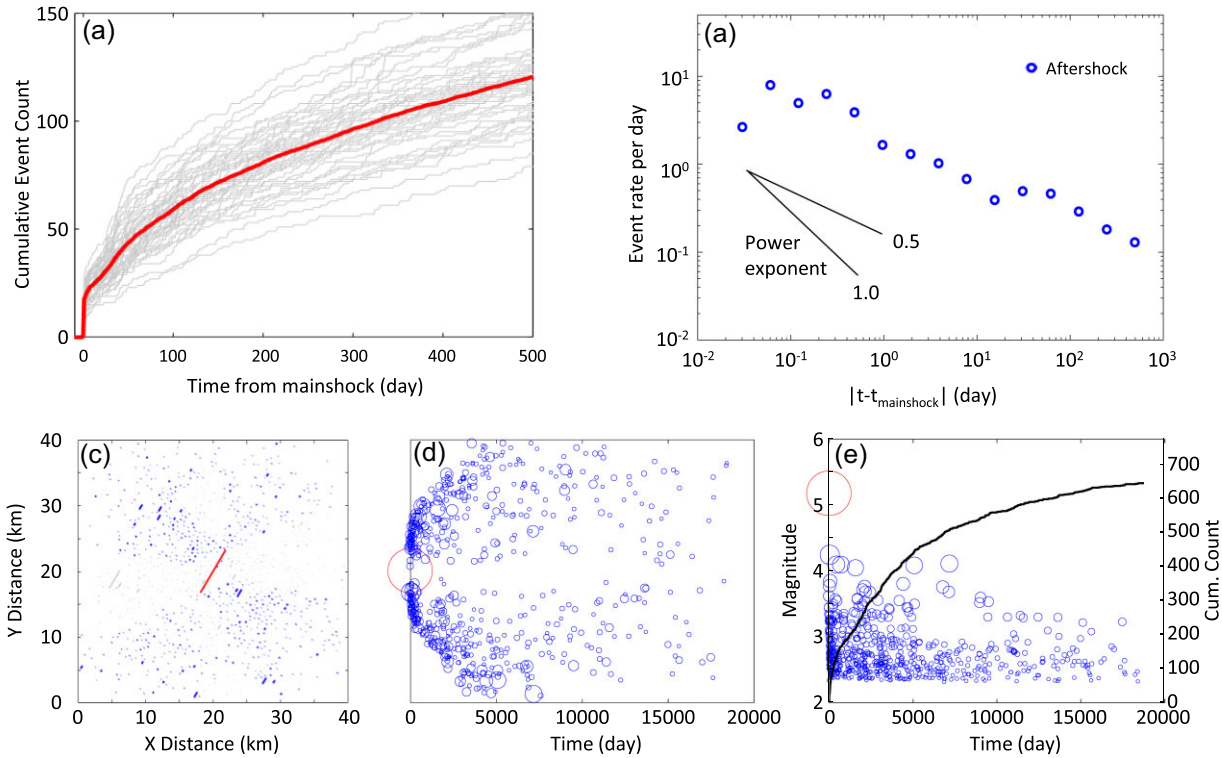

Figure 11. Simulation results in the case of identical initial velocity (except for the main fault, which is assumed to have a higher initial velocity), and no complex fault zone. (a) Cumulative seismicity with time. Grey lines show all simulation results, and the bold red line denotes the stacked average. (b) Event rate versus time from the mainshock. (c–g) Detailed simulation result of one selected case. (c) Fault geometry. The coloured faults ruptured during our simulation (main fault in red), whereas the grey faults are not. (d) Event location versus time for all events. (e) Event magnitude and cumulative count for all events.

and Gutenberg–Richter laws. We use the algorithm of Ogata (1988), which assumes that the seismicity results from the sum of independent background events and events triggered by previous events. The seismicity rate is then

$$\lambda(t) = \mu_0 + \sum_{i|t_i<t} K10^{\alpha(M_i-M_c)}(t - t_i + c)^{-(1+\phi)}, \quad (23)$$

where M_i is the magnitude of ith seismic event, M_c is the minimum magnitude of earthquake contributing to the cascading process, t is time and α, K, c and ϕ are parameters (here ϕ is commonly written as θ in literatures). The first term on the right-hand side, μ_0, is background seismicity taken as a random process. The summation account for the direct aftershocks of each event i. The term $K10^{\alpha(M_i-M_c)}$ represents magnitude-dependent aftershock productivity—a higher magnitude of the mother event (M_i) gives higher intensity. The term $(t - t_i + c)^{-(1+\phi)}$ represents the 'local' Omori decay of direct aftershocks with local $p = 1 + \phi$ (Helmstetter & Sornette 2002). The magnitude of aftershocks is randomly selected based on the Gutenberg–Richter frequency distribution.

ETAS is a branching model that can lead to rich dynamics depending on the model parameters (Helmstetter & Sornette 2002). The branching ratio can be lower than 1, leading to a subcritical regime, where the number of aftershocks triggered directly or indirectly from single mainshock decays to zero. It can also be larger than 1, leading to a supercritical regime, where an infinite number of earthquakes are triggered over a finite time. The branching ratio is determined by ETAS parameters and is always supercritical when $\phi \leq 0$ (Helmstetter & Sornette 2002).

The difference between the DFN simulation result and the ETAS can be evaluated by finding the ETAS parameters that best describe our simulation results. To find the parameters, we conducted two inversions: (i) by fitting the stacked seismicity curves or (ii) by applying the maximum likelihood estimation (MLE) method to the synthetic seismicity catalogues. The two methods yield consistent results regarding the effect of earthquake interactions on the ETAS parameters characterizing the productivity of earthquake triggering (K and α). Here we present the results obtained using the first method. The MLE inversion results are presented in the supplementary material (Text S1 and Table S1).

We conducted ETAS simulations with 'AftSimulator.m' (Felzer *et al.* 2002) with a setup designed to match our discrete fault network simulations. We set the minimum magnitude to $M_c = 2.5$, the maximum magnitude to $M_{\max} = 5.5$, and the background seismicity to $\mu_0 = 0.0356$ (13 events yr^{-1}). The simulated time is 10 yr. We selected the simulations with a maximum magnitude larger than M 4.0. Hence, the mainshocks in the selected simulations are within the range of M 4.0–5.5, which corresponds to the range of magnitude of the mainshock events in our discrete fault network simulations. We also discarded the mainshock rupture simulations within 500 d from the beginning or 500 d from the end of the simulation to avoid truncating the foreshock and aftershock sequence. The simulation was repeated until we had 1000 mainshocks that met the above criteria. The cumulative seismicity of all simulations was stacked and averaged (Fig. 12). We determined the best-fitting parameters α, K, c and ϕ from trial and error.

We initially aimed to find the parameter set fitting the evolution of our stacked simulations during both the foreshock and aftershock sequences (Fig. 12). However, we were unable to fit well both foreshocks and aftershocks and decided to fit either one or the other. Fig. 12(a) shows the ETAS model fitting the aftershocks best. Individual ETAS simulations have a wider range of cumulative event counts than our discrete fault network simulations. The cumulative event often goes well beyond 400 events (Fig. 12a grey lines). This high event count cannot be reached in our discrete fault simulation (Fig. 8a). Because our discrete fault simulation has a limited number of faults, the number of critically stressed faults decreases as faults rupture. Although a single fault can repeatedly rupture due to stress transfer among faults, the seismicity rate increase is nonetheless bounded due to the fact that nucleation is not instantaneous. The ETAS model does not have these physical limits. Therefore, the cumulative event number is not bounded in principle. However, once stacked, the ETAS simulation well matches our discrete fault simulation aftershock sequence (Fig. 12a).

The ETAS model fitting best the aftershocks [$c = 0.01$, $\phi = 0.20$ ($p = 1.2$), $K = 0.011$] does not fit the foreshocks well. In the ETAS simulation, the foreshock rate starts to accelerate only 10–20 days before the mainshock (Fig. 12a blue line). The discrete fault simulation shows a more pronounced and longer period of foreshock acceleration (Fig. 12a, inset). For ETAS to fit the foreshock sequence, the productivity must be double (Fig. 12b) so that an earthquake can potentially trigger about twice as many events. To compensate for this high productivity, we had to reduce the background seismicity rate by half. However, in this case, the ETAS model does not fit well with the aftershocks (Fig. 12b).

Compared to the dense fault zone case, the discrete fault simulations with no dense fault zone case (Fig. 9) show an opposite end-member behaviour. Foreshock acceleration is almost entirely absent (Fig. 9b). Instead, the foreshock rate stays at the initial seismicity rate (13 events yr^{-1}). This behaviour can be reproduced in ETAS simulations if low productivity (K) is assumed (Fig. 13). However, similarly to the complex fault zone case (Fig. 12), low productivity also reduces aftershock productivity, so the ETAS simulations are then unable to fit the aftershocks produced in our discrete fault simulation (Fig. 13a). The number of aftershocks becomes more significant as K increases, but foreshocks are then ill-fitted (Fig. 13a).

Our best-fitting ETAS model [Figs 13b and c; $\phi = -0.2$ ($p = 0.8$), $\alpha = 1$ and $K = 0.007$] has a much lower background seismicity rate ($\lambda_0 = 1.9$ event yr^{-1}) than the input rate of the discrete fault simulation (13 event yr^{-1}) because most events are due to interactions which do not occur in our discrete fault network simulations because of the finite number of faults. Note that the ETAS parameter $\phi = -0.2$ ($p = 0.8$) implies a supercritical behaviour (Helmstetter & Sornette 2002). Therefore, it is non-physical, as the seismicity rate would diverge to infinity at a finite time in longer-term simulations. Within the 10-yr span of our ETAS simulations, a burst of aftershocks occasionally occurs, leading to a much larger increase in seismicity rate than observed in our simulation. This difference is again due to the limited number of faults involved in the generation of the aftershock sequence in the discrete fault simulation with a sparse fault network.

The foreshock and aftershock productivity in the discrete fault simulations is thus significantly influenced by fault distributions in the main fault zone and the background area. The foreshocks are mostly located in the main fault zone (Fig. 5c), whereas the aftershocks are widely distributed over the simulation domain, implying that the magnitude of earthquake interactions, which is represented by the productivity in the ETAS model, is not necessarily, or unlikely, equal between foreshocks and aftershocks.

6. DISCUSSION

The discrete fault presented in this study is essentially a Coulomb Rate and State (CRS) model (e.g. Stein *et al.* 1997; Stein 1999;

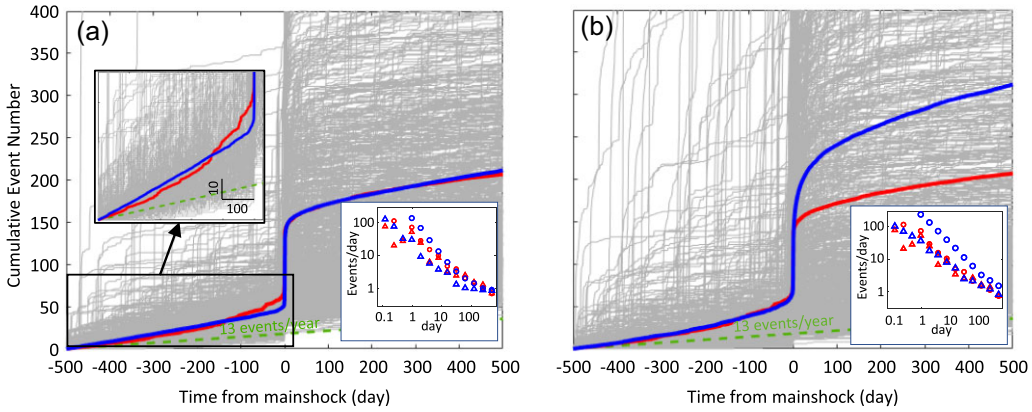

Figure 12. Comparison of the time evolution of seismicity obtained from our discrete fault network simulations (red line) with ETAS simulations for either the foreshocks (a) or the aftershocks (b) of the maximum event in the catalogue. Grey lines denote 1000 individual ETAS simulations. The bold blue line denotes the stacked average of the ETAS simulation. The bold red line denotes stacked discrete fault simulation with a complex fault zone (identical to Fig. 8a red line). The best-fitting models correspond to $\mu_0 = 13$ event yr^{-1}, $c = 0.0015$, $\phi = 0.261$ ($p = 1.261$), $K = 0.005$ and $\alpha = 1$ for the aftershock (a), and $\mu_0 = 6.5$ event yr^{-1}, $c = 0.01$, $\phi = 0.20$ ($p = 1.2$), $K = 0.011$ and $\alpha = 1$ for the foreshock (b). Insets: time versus event rate with circles denoting aftershock, triangles denoting foreshock, red colours denoting stacked simulation result, and blue colours denoting ETAS result. See Fig. S6 for additional fitting test results.

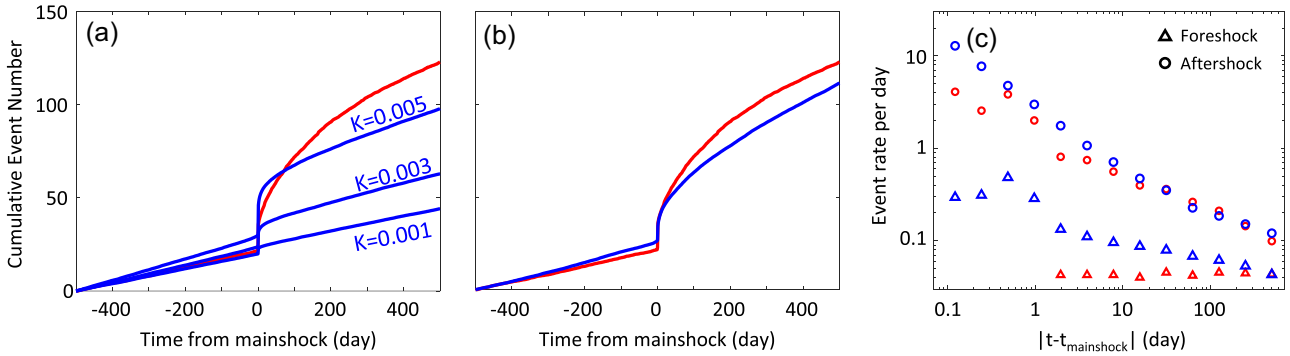

Figure 13. Comparison of the time evolution of seismicity obtained from our discrete fault network simulations with no complex fault zone case (red line, identical to the red line in Fig. 9a) with ETAS simulations (blue lines). (a) $\lambda_0 = 13$ event yr^{-1}, $\phi = 0$ ($p = 1.0$), $\alpha = 1$ and with varied K. (b) One of our best-fitting models to both foreshocks and aftershocks. $\lambda_0 = 1.9$ event yr^{-1}, $\phi = -0.2$ ($p = 0.8$), $\alpha = 1$ and $K = 0.007$. The parameter set is in the supercritical regime (Helmstetter & Sornette 2002), meaning that the number of daughter events exceeds the number of mother events. (c) Time versus event rate of the best fitting model (b) with circles denoting aftershock, triangles denoting foreshock, red colours denoting stacked simulation result and blue colours denoting ETAS result.

Segou *et al.* 2013) with an explicitly defined network of pre-existing faults of finite size allowing for stress interactions. Our study confirms previous works (Ziv 2003; Dieterich & Richards-Dinger 2010; Ozawa & Ando 2021), which show that, just like the ETAS model (Helmstetter *et al.* 2003), a discrete network of faults governed by rate and state friction can produce aftershocks and foreshocks as a result of cascades of triggered earthquakes. Our simulation method can accommodate various fault network geometries, allowing to investigate the role of fault zone complexity in the earthquake sequence and to compare the result with the ETAS model.

The stacked sequence of foreshocks produced by these two different approaches—discrete fault network and ETAS—resembles natural examples. They show a power-law acceleration, an inverse Omori law, and a spatial migration towards the mainshock. ETAS has therefore been used as a standard to identify foreshock sequences that seem inconsistent with a cascading process and might reflect a nucleation process involving some aseismic slip (McGuire *et al.* 2005; Bouchon *et al.* 2013). In such instances, foreshocks could eventually provide information about the preparation for large earthquakes (Kato & Ben-Zion 2021). Because geodetic data are rarely available or might not provide enough resolution, identifying such anomalous foreshock sequences in the seismicity catalogue is important. ETAS might seem to be a good tool for this application. This approach then assumes that the triggering process reflected in the aftershocks sequences, which dominate seismicity catalogues and are represented by the ETAS algorithm, applies to foreshocks as well. There are, however, substantial differences in the cascading process modelled using ETAS or our discrete fault network model. These differences are due to the fact that ETAS is purely statistical and, therefore, not constrained to be consistent with the physics incorporated in our discrete fault model, as we discuss later.

6.1 Earthquake cascades in a discrete fault network and ETAS

Both the ETAS and discrete fault network models allow one earthquake to trigger another, allowing for cascades of an earthquake to form. In both models, as implemented in this study, the magnitude of a triggered earthquake is not conditioned by the magnitude of the triggering event. This allows for foreshocks. There are, however, material differences between the two models. The most fundamental one is that earthquakes occur on a finite number of interacting

faults in the discrete fault network model. Any event produces both positive and negative static stress changes on all other faults, resulting in time advances or delays. In our simulations, the main fault typically experiences multiple stress changes before rupture (e.g. Figs 5h and i). So, each earthquake is influenced by all previous events and is drawn from a finite pool of faults. The discrete fault network model implies temporal and spatial variability in the productivity of cascades of seismicity. The productivity is reduced after the mainshock rupture due to the depletion of the critically stressed fault (Fig. 12) and is larger where faults are more closely packed, leading to larger stress transfers. By contrast, the ETAS model is an unbounded additive process with a mother–daughter relationship, where a daughter can have only one mother. In addition, the productivity of cascade is generally assumed constant in time and uniform in space.

6.2 Productivity difference between foreshock and aftershock sequence

Foreshock and aftershock have different statistical properties (e.g. Chen & Shearer 2013; Gulia & Wiemer 2019). Our work points out one possible important cause for these differences. As expected from our analytical mean-field approximation, the foreshocks are enhanced if interactions among the faults are stronger. This condition can be met if the main fault is embedded in a complex fault zone with high-density faulting. Conversely, aftershock occurs everywhere in the simulation domain, including the low-density surrounding area, where interaction is weak. As a result, the productivity will drop temporally, leading to apparently lower productivity during the aftershock sequence.

Accordingly, the ETAS model cannot reproduce our result if the productivity parameter is constant between the foreshock and aftershock (Figs 12, 13 and S5, Text S1). Our sensitivity test and MLE inversion clearly show that no single set of model parameters unlikely can fit both. This can be reasonably explained by fault interactions in our discrete fault model. The ETAS productivity represents the likelihood of a mother event triggering daughter events. Accordingly, it should be higher in case of stronger interactions within a denser population of faults. In our simulations, the foreshocks occur within a higher density complex fault zone, whereas aftershock occurs all over a broader simulation domain with a lower density of faults (Figs 5b and c). Therefore, if the fault zone is complex, high ETAS productivity in the foreshock is expected (Fig. 12), and conversely, if the fault zone is least complex, low ETAS productivity in the foreshock is expected (Fig. 13). This is well presented in Fig. 10, which shows that the foreshock p-value is strongly dependent on the fault network geometry, whereas the aftershock p-value is not. Our work suggests that the foreshock sequence is controlled by the various geometry of fault zone structures observed in natural fault systems (Ben Zion & Sammis 2003; Faulkner *et al.* 2010; Savage & Brodsky 2011).

Our work suggests that earthquake productivity should not be considered identical for foreshock and aftershock sequences. The observation of an anomalously high productivity of foreshocks compared to the ETAS standard might, therefore, not necessarily imply that cascading should be discarded. Our simulation result suggests that the discrepancy between the observation and the ETAS can come from the assumption of 'constant' productivity.

6.3. Relaxing the assumption of the Dieterich (1994) model regarding the cause of the Omori law

As noted in some previous studies (Ziv 2003; Ozawa & Ando 2021), the specific initial velocity distribution assumed by Dieterich (1994) is not essential to obtain aftershock sequences consistent with the Omori law in a discrete fault network model. In our simulations, the Omori law emerges due to the heterogeneous stress change distribution imparted by previous earthquakes and is, therefore, also independent of the initial velocity distribution (Figs 2 and 11), or equivalently independent of the initial stress distribution. In our simulations, the heterogeneity of stress is maintained by fault interactions. Fault interactions could also play an important role in the emergence of the Omori law in nature.

6.4. Role of aseismic creep and in mechanism of foreshock—cascade and pre-slip.

Our results show that earthquake cascades in a discrete fault network produce realistic swarms, foreshock and aftershock sequences, but in reality, aseismic slip might be an additional mechanism of clustering or even a prevailing one in some cases. Our model includes the effect of aseismic pre-slip associated with the nucleation process, which is theoretically predicted (Dieterich 1992), but this effect is negligible in our model as the stress changes associated with the nucleation phase are very small compared to the coseismic stress changes. Aseismic slip can also occur in the form of afterslip on rate-strengthening fault patches (Marone *et al*. 1991) and contribute to triggering aftershocks (*e.g.* Perfettini & Avouac 2004; Hsu *et al.* 2006; Cattania *et al.* 2015) and swarms (*e.g.* Vidale & Shearer 2006; Lohmann & McGuire 2007; Llenos *et al.* 2009; Ross *et al.* 2017; Sirorattanakul *et al.* 2022). It is probable that friction is not homogeneous, even at the scale of a single fault where rate weakening and rate strengthening patches could intermingle (e.g. Bedford *et al.* 2022) and help explain the aftershocks (Perfettini & Avouac 2007; Dublanchet *et al*. 2013) and foreshocks (Dublanchet 2018) characteristics. In that case, aseismic slip help mediate or enhance earthquake interactions (Cattania & Segall 2021).

It is, therefore, possible that earthquake triggering is mediated by aseismic slip in nature much more than our model allows due to fault roughness or frictional heterogeneity. Including this effect would probably not change the main findings of this study as it would essentially modify the mechanisms of fault interactions leading to probably a similar qualitative behaviour. We do not question that there are instances where aseismic pre-slip has driven foreshocks, swarms or foreshocks. We, however, note that an abundance of foreshocks, compared to expectations from ETAS, might not necessarily require pre-slip.

6.5. On the role of interevent interactions in swarms

Seismicity swarms are commonly interpreted to be driven by transient loading due to aseismic slip (e.g. Vidale & Shearer 2006; Lohmann & McGuire 2007; Llenos *et al.* 2009; Sirorattanakul *et al.* 2022), fluid flow (Ross *et al*. 2020; Cebry *et al*. 2022) or both (Ross *et al.* 2017). However, our simulations demonstrate that swarm-like migrating clusters can result from cascading alone in a Discrete Fault Network model, as it can happen in ETAS simulations as well (Helmstetter & Sornette 2002). Identifying the role of stress transfers in swarms based on seismicity catalogues is a challenge as it is impossible to see the complete chain of interactions due to the missing events with a magnitude lower than the magnitude of detection,

which are necessarily dominant by virtue of the Gutenberg–Richter law. Vidale & Shaerer (2006) argued that cascading plays a minor role in driving swarms based on their observations which included: 'the presence of an interval of steady seismicity rate, the tendency of the largest event to strike later in the sequence, the large spatial extent of some of the swarms compared to their cumulative moment, and the weak correlation between the number of events in each burst and the magnitude of the largest event in each burst'. Cascading is probably not the dominant mechanism at the origin of swarms in nature, but it could play a role in addition to transient loading or fluid flow. For example, during the Westmorland swarm, which was mostly driven by a slow slip event measured from GNSS and SAR interferometry, it seems that 10–30 per cent of the events were due to earthquake interactions (Sirorattanakul *et al.* 2022). The observation of a swarm might, therefore, not necessarily indicate fluid flow or an aseismic transient.

6.6. Ageing law versus slip law

We also conducted a slip evolution law simulation for the reference simulation with identical setups. The most significant difference between the two simulations is that, with the slip law, the velocity change is much faster during the quasi-static acceleration phase and that the faults are more sensitive to stress change. For example, in our test simulations (Figs 3 and S1), the mainshock rupture (black fault) occurs at ∼470 s for the ageing law and ∼30 s for the slip law. And the green fault rupture occurs ∼150 s after the mainshock for ageing law and ∼10 s after the mainshock for slip law. The simulation for our reference discrete fault network with the slip law results in a similar difference. The seismicity rate before the mainshock is ∼13 events yr $^{-1}$ for the ageing law (Fig. 5e) and is ∼100 events yr^{-1} for the slip law (Fig. S2e). Slip law simulation also shows foreshocks (Fig. S2), but the foreshock sequences are much shorter than with the ageing law simulations. In both cases, the foreshock sequence was triggered by a green fault (Figs 5i and S2i). It only took ∼0.006 d (∼8 min) from the beginning of the immediate foreshock sequence to mainshock rupture for slip law (Fig. S2i), whereas it took 0.3 d (∼7.2 hr) for ageing law (Fig. 5i).

Despite the differences, the slip law simulations are qualitatively comparable to those run with the ageing law. Both laws show multiple foreshocks before the mainshock. Both laws show the Omori law aftershock decay (Fig. 6). Thus, at least in our simulations, it seems that both laws can qualitatively reproduce natural observation.

7. CONCLUSION

We have used a discrete fault network and some analytical approximations to explore how interactions among faults obeying rate and state friction lead to earthquake cascades in the form of foreshock and aftershock sequences and eventually swarms. The formation of cascades results from the time advance of ruptures of a finite number of faults due to static stress transfer. This effect is therefore enhanced if the fault network is dense. Aftershock sequences in such a model systematically follow the Omori law due to the heterogeneity of Coulomb stress changes. Similarly, foreshock sequences follow an inverse Omori law. These results confirm observations made in previous studies that have adopted a discrete or inherently discrete modelling approach (Ziv 2003; Ziv & Rubin 2003; Ozawa & Ando 2021).

The collective dynamics emerging from fault interactions in a discrete fault network resemble the dynamics that can emerge from ETAS (Helmstetter & Sornette 2002; Helmstetter *et al.* 2003). However, the cascading process in a discrete fault network is not equivalent to the cascading process in ETAS, which is additive and unbounded. In a discrete fault network, the topology of the network and the temporal depletion of critically stressed faults can enhance foreshocks compared to the expectation based on the ETAS model calibrated with aftershocks. This finding implies that an abundance of foreshocks anomalously high compared to the expectation based on ETAS, as reported in particular for large subduction earthquakes (Bouchon *et al.* 2013), may not necessarily require another mechanism (i.e. pre-slip) than cascading. It can also originate from more productive foreshock cascades in complex fault zones, as happens in our simulations. Note that our model only accounts for the cascading process resulting from static coseismic stress transfer and cannot be used to predict the occurrence time or magnitude of a large shock. This would require exact knowledge of the fault network geometry, properties and initial conditions. It remains, however, true that the significance of cascading foreshocks, possibly favoured by a complex fault zone with a high density of secondary faults, increases before a larger mainshock event. This statistical effect could be the basis for time-dependent probabilistic earthquake forecasting.

Progressive localization of the seismicity might precede large earthquakes (see Kato & Ben-Zion 2021, for review). This view expands the usual notion of foreshocks in that the localization process results from a combination of increasing seismicity around the mainshock area and decreasing seismicity farther away. Kato & Ben-Zion (2021) suggest that this observation would be due to shear localization governed by the evolution of rock damage. This idea is not explored in our study as the possible effect of rock damage evolution is not incorporated into our model.

SUPPORTING INFORMATION

Supplementary data are available at *GJI* online.

Figure S1. Identical to Fig. 3 but with slip law.

Figure S2. Identical to Fig. 5 but with slip law.

Figure S3. Simulation results with constant loading. The panel descriptions are identical to Figs 5(a)–(f) of the main text. Fault distribution is randomly set with the identical method for the main simulation setup (complex fault zone simulation, Section 3.3). We used constant shear stressing throughout the simulation period at 10 kPa yr^{-1}, which roughly corresponds with the interseismic loading rate of the south California San Andreas fault (Freed *et al.* 2007). Initial velocity is randomly set by equation 17 (case with loading) to yield ∼23 events yr^{-1} when no interaction is assumed. Cascading foreshock is apparent a few days before the mainshock. The result is essentially similar to Fig. 5, which assumed no loading.

Figure S4. Stacked results from simulations with tectonic loading included (10 kPa yr^{-1}, *cf.* Fig. S3). We conducted 100 simulations. Among them, 31 simulations that have the mainshock after 500 d are selected and stacked. The simulation parameters are identical to Fig. S3 but with randomized geometry. (a) Cumulative seismicity with time before and after the mainshock. Grey lines denote 31 simulation results that have mainshock occurring after 500 d. Fig. S3 case is highlighted in the black line. The bold red line denotes the stacked average. (b) Event rate versus time form mainshock for both foreshock (black triangle) and aftershock (blue circles). The green dashed line denotes the seismicity rate in the case of no cascading interaction.

Figure S5. Cumulative seismicity with time before and after the mainshock for simulations with an initial number of faults in the

fault zone of 50 (a), 100 (b) and 150 (c). The remaining number of faults after the application of the 'too close' criterion is 42 (a), 78 (b) and 108 (c). Grey lines show all simulation results, and bold red lines denote the stacked average.

Figure S6. Additional attempts to fit foreshock (c, d) and aftershock (a, b) sequences in our discrete fault network model with ETAS. This figure corresponds to Fig. 12 but with different parameters. (a) $\lambda_0 = 13$ event yr^{-1}, $c = 0.028$, $\theta = 0.3$ ($p = 1.3$), $K = 0.011$ and $\alpha = 1$. (b) $\lambda_0 = 13$ event yr^{-1}, $c = 0.015$, $\theta = 0.3$ ($p = 1.3$), $K = 0.011$ and $\alpha = 0.945$. (c) $\lambda_0 = 6.5$ event yr^{-1}, $c = 0.001$, $\theta = 0.3$ ($p = 1.3$), $K = 0.005$ and $\alpha = 1$. (d) $\lambda_0 = 4.68$ event yr^{-1}, $c = 0.0005$, $\theta = 0.1$ ($p = 1.1$), $K = 0.01$ and $\alpha = 0.93$.

Table S1. MLE parameter inversion result.

Please note: Oxford University Press is not responsible for the content or functionality of any supporting materials supplied by the authors. Any queries (other than missing material) should be directed to the corresponding author for the paper.

ACKNOWLEDGMENTS

We thank three anonymous reviewers for their insightful and constructive evaluations. This study was supported by the National Science Foundation (award #1822214) via the IUCR centre Geomechanics and Mitigation of Geohazards.

CONFLICT OF INTEREST

The authors have no conflicts of interest to declare.

DATA AVAILABILITY

The discrete fault simulator is available at https://github.com/limkjae/MDFNRSF2D. No new data were generated or analysed in support of this research.

REFERENCES

Bedford, J. D., Faulkner, D. R. & Lapusta, N., 2022. Fault rock heterogeneity can produce fault weakness and reduce fault stability, *Nat. Commun.,* **13**(1), 326.

Ben-Zion, Y. & Sammis, C. G., 2003. Characterization of fault zones, *Pure appl. Geophys.,* **160**(3), 677–715.

Bouchon, M., Durand, V., Marsan, D., Karabulut, H. & Schmittbuhl, J., 2013. The long precursory phase of most large interplate earthquakes, *Nat. Geosci.,* **6**(4), 299–302.

Cattania, C., Hainzl, S., Wang, L., Enescu, B. & Roth, F., 2015. Aftershock triggering by postseismic stresses: a study based on coulomb rate-and-state models, *J. geophys. Res,* **120**(4), 2388–2407.

Cattania, C., Hainzl, S., Wang, L., Roth, F. & Enescu, B., 2014. Propagation of coulomb stress uncertainties in physics-based aftershock models, *J. geophys. Res,* **119**(10), 7846–7864.

Cattania, C. & Segall, P., 2021. Precursory slow slip and foreshocks on rough faults, *J. geophys. Res,* **126**(4), e2020JB020430, doi:10.1029/2020JB020430.

Cebry, S. B. L, Ke, C.-Y. & McLaskey, G. C. 2022. The role of background stress state in fluid-induced aseismic slip and dynamic rupture on a 3-m laboratory fault, *Journal of Geophysical Research: Solid Earth,* **127,** e2022JB024371. https://doi.org/10.1029/2022JB024371.

Chen, K., Avouac, J.-P., Aati, S., Milliner, C., Zheng, F. & Shi, C., 2020. Cascading and pulse-like ruptures during the 2019 Ridgecrest earthquakes in the Eastern California Shear Zone, *Nat. Commun.,* **11**(1), doi:10.1038/s41467-019-13750-w.

Chen, X. & Shearer, P. M., 2013. California foreshock sequences suggest aseismic triggering process, *Geophys. Res. Lett.,* **40**(11), 2602–2607.

Chen, X. & Shearer, P. M., 2016. Analysis of foreshock sequences in California and implications for earthquake triggering, *Pure appl. Geophys.,* **173**(1), 133–152.

Crouch, S. L., 1976. Solution of plane elasticity problems by the displacement discontinuity method. I. Infinite body solution, *Int. J. Numer. Methods Eng.,* **10**(2), 301–343.

Dieterich, J. H., 1979. Modeling of rock friction: 1. Experimental results and constitutive equations, *J. geophys. Res.,* **84**(9), 2161–2168.

Dieterich, J. H., 1992. Earthquake nucleation on faults with rate-and state-dependent strength, *Tectonophysics,* **211**(1–4), 115–134.

Dieterich, J. H., 1994. A constitutive law for rate of earthquake production and its application to earthquake clustering, *J. geophys. Res,* **99**(B2), 2601–2618.

Dieterich, J. H. & Richards-Dinger, K. B., 2010 Earthquake recurrence in simulated fault systems, *Pure appl. Geophys.,* **167,** 1087–1104.

Dodge, D. A., Beroza, G. C. & Ellsworth, W. L., 1996. Detailed observations of California foreshock sequences: implications for the earthquake initiation process, *J. geophys. Res,* **101**(B10), 22 371–22 392.

Dublanchet, P., 2018 The dynamics of earthquake precursors controlled by effective friction, *Geophys. J. Int.,* **212,** 853–871.

Dublanchet, P., 2022. Seismicity modulation in a 3-D rate-and-state interacting fault population model, *Geophys. J. Int.,* **229**(3), 1804–1823.

Dublanchet, P., Bernard, P. & Favreau, P., 2013 Creep modulation of Omori law generated by a Coulomb stress perturbation in a 3-D rate-and-state asperity model, *J. geophys. Res.,* **118,** 4774–4793.

Ellsworth, W. L. & Bulut, F., 2018. Nucleation of the 1999 Izmit earthquake by a triggered cascade of foreshocks, *Nat. Geosci.,* **11**(7), 531–535.

Enescu, B., Mori, J. & Miyazawa, M., 2007. Quantifying early aftershock activity of the 2004 mid-Niigata Prefecture earthquake (M(w)6.6), *J. geophys. Res.,* **112**(B4), doi:10.1029/2006JB004629.

Faulkner, D. R., Jackson, C. A. L., Lunn, R. J., Schlische, R. W., Shipton, Z. K., Wibberley, C. A. J. & Withjack, M. O., 2010. A review of recent developments concerning the structure, mechanics and fluid flow properties of fault zones, *J. Struct. Geol.,* **32**(11), 1557–1575.

Felzer, K. R., Becker, T. W., Abercrombie, R. E., Ekström, G. & Rice, J. R., 2002. Triggering of the 1999 Mw 7.1 Hector Mine earthquake by aftershocks of the 1992 Mw 7.3 Landers earthquake, *J. geophys. Res,* **107**(B9), ESE 6–1-ESE 6-13.

Frank, W. B., Poli, P. & Perfettini, H., 2017, Mapping the rheology of the Central Chile subduction zone with aftershocks, *Geophys. Res. Lett.,* **44**(11), 5374–5382.

Freed, A. M., Ali, S. T. & Bürgmann, R., 2007. Evolution of stress in Southern California for the past 200 years from coseismic, postseismic and interseismic stress changes, *Geophys. J. Int.,* **169**(3), 1164–1179.

Gomberg, J., 2001. The failure of earthquake failure models, *J. geophys. Res,* **106**(B8), 16 253–16 263.

Gulia, L. & Wiemer, S., 2019. Real-time discrimination of earthquake foreshocks and aftershocks, *Nature,* **574**(7777), 193–199.

Hardebeck, J. L., 2021. Spatial clustering of aftershocks impacts the performance of physics-based earthquake forecasting models, *J. geophys. Res,* **126**(2), e2020JB020824, doi:10.1029/2020JB020824.

Harris, R. A., 1998. Introduction to special section: stress triggers, stress shadows, and implications for seismic hazard, *J. geophys. Res,* **103**(B10), 24 347–24 358.

Heimisson, E. R., 2019. Constitutive law for earthquake production based on rate-and-state friction: theory and application of interacting sources, *J. geophys. Res,* **124**(2), 1802–1821.

Heimisson, E. R. & Segall, P., 2018. Constitutive law for earthquake production based on rate-and-state friction: Dieterich 1994 revisited, *J. geophys. Res,* **123**(5), 4141–4156.

Helmstetter, A. & Shaw, B. E., 2006. Relation between stress heterogeneity and aftershock rate in the rate-and-state model, *J. geophys. Res,* **111**(B7), doi:10.1029/2005JB004077.

Helmstetter, A. & Sornette, D., 2002. Subcritical and supercritical regimes in epidemic models of earthquake aftershocks, *J. geophys. Res,* **107**(B10), ESE 10–1-ESE 10-21.

Helmstetter, A., Sornette, D. & Grasso, J.-R., 2003. Mainshocks are aftershocks of conditional foreshocks: how do foreshock statistical properties emerge from aftershock laws, *J. geophys. Res,* **108**(B1), doi:10.1029/2002JB001991.

Hsu, Y.-J., Simons, M., Avouac, J.-P., Galetzka, J., Sieh, K., Chlieh, M., Natawidjaja, D., Prawirodirdjo, L. & Bock, Y., 2006. Frictional afterslip following the 2005 Nias-Simeulue Earthquake, Sumatra, *Science,* **312**(5782), 1921–1926.

Im, K. & Avouac, J.-P., 2021. Tectonic tremor as friction-induced inertial vibration, *Earth planet. Sci. Lett.,* **576,** 117238.

Im, K., Elsworth, D., Marone, C. & Leeman, J., 2017. The impact of frictional healing on stick-slip recurrence interval and stress drop: implications for earthquake scaling, *J. geophys. Res.,* **122**(12), 10 102–10 117.

Jones, L. M. & Molnar, P., 1979. Some characteristics of foreshocks and their possible relationship to earthquake prediction and premonitory slip on faults, *J. geophys. Res,* **84**(B7), 3596–3608.

Kagan, Y. Y. & Houston, H., 2005. Relation between mainshock rupture process and Omori's law for aftershock moment release rate, *Geophys. J. Int.,* **163**(3), 1039–1048.

Kagan, Y. Y. & Knopoff, L., 1981. Stochastic synthesis of earthquake catalogs, *J. geophys. Res,* **86**(B4), 2853–2862.

Kato, A. & Ben-Zion, Y., 2021. The generation of large earthquakes, *Nat. Rev. Earth Environ.,* **2**(1), 26–39.

Kato, A., Obara, K., Igarashi, T., Tsuruoka, H., Nakagawa, S. & Hirata, N., 2012. Propagation of slow slip leading up to the 2011 Mw 9.0 Tohoku-Oki earthquake, *Science,* **335**(6069), 705–708.

Kilb, D., Martynov, V. G. & Vernon, F. L., 2007. Aftershock detection thresholds as a function of time: results from the ANZA Seismic Network following the 31 October 2001 ML 5.1 Anza, California earthquake, *Bull. seism. Soc. Am.,* **97,** 780–792.

King, G. C. P., Stein, R. S. & Lin, J., 1994. Static stress changes and the triggering of earthquakes, *Bull. seism. Soc. Am.,* **84**(3), 935–953.

Llenos, A. L., McGuire, J. J. & Ogata, Y., 2009. Modeling seismic swarms triggered by aseismic transients, *Earth planet. Sci. Lett.,* **281**(1–2), 59–69.

Lohman, R. B. & McGuire, J. J., 2007. Earthquake swarms driven by aseismic creep in the Salton Trough, California, *J. geophys. Res,* **112**(B4), doi:10.1029/2006JB004596.

Lomax, A., 2020. Absolute location of 2019 Ridgecrest seismicity reveals a shallow Mw 7.1 hypocenter, migrating and pulsing Mw 7.1 foreshocks, and Duplex Mw 6.4 ruptures, *Bull. seism. Soc. Am.,* **110**(4), 1845–1858.

Mancini, S., Segou, M., Werner, M. J. & Cattania, C., 2019. Improving physics-based aftershock forecasts during the 2016–2017 Central Italy Earthquake Cascade, *J. geophys. Res,* **124**(8), 8626–8643.

Marone, C. J., Scholtz, C. H. & Bilham, R., 1991. On the mechanics of earthquake afterslip, *J. geophys. Res,* **96**(B5), 8441–8452.

Marone, C., 1998. Laboratory-defived friction laws and their application to seismic faulting, *Annu. Rev. Earth planet. Sci.,* **26**(1), 643–696.

Marsan, D., 2005. The role of small earthquakes in redistributing crustal elastic stress, *Geophys. J. Int.,* **163**(1), 141–151.

Marsan, D., 2006. Can coseismic stress variability suppress seismicity shadows? Insights from a rate-and-state friction model, *J. geophys. Res,* **111**(B6), doi:10.1029/2005JB004060.

Marsan, D. & Lengline, O., 2008, Extending earthquakes' reach through cascading, *Science,* **319**(5866), 1076–1079.

McGuire, J. J., Boettcher, M. S. & Jordan, T. H., 2005. Foreshock sequences and short-term earthquake predictability on East Pacific Rise transform faults, *Nature,* **434**(7032), 457–461.

McLaskey, G. C., 2019. Earthquake initiation from laboratory observations and implications for foreshocks, *J. geophys. Res,* **124**(12), 12 882–12 904.

Meier, M., Werner, M. J., Woessner, J. & Wiemer, S., 2014. A search for evidence of secondary static stress triggering during the 1992 M_w 7.3 Landers, California, earthquake sequence, *J. geophys. Res,* **119**(4), 3354–3370.

Miller, S. A., Collettini, C., Chiaraluce, L., Cocco, M., Barchi, M. & Kaus, B. J. P., 2004. Aftershocks driven by a high-pressure CO_2 source at depth, *Nature,* **427**(6976), 724–727.

Mogi, K., 1963. Some discussions on aftershocks, foreshocks and earthquake swarms: the fracture of a semi-infinite body caused by an inner stress origin and its relation to the earthquake phenomena (third paper), *Bull. Earthq. Res. Inst., Univ. Tokyo,* **41**(3), 615–658.

Moutote, L., Marsan, D., Lengliné, O. & Duputel, Z., 2021. Rare occurrences of non-cascading foreshock activity in Southern California, *Geophys. Res. Lett.,* **48**(7), e2020GL091757, doi:10.1029/2020GL091757.

Nur, A. & Booker, J. R., 1972. Aftershocks caused by pore fluid flow?, *Science,* **175**(4024), 885–887.

Ogata, Y., 1988. Statistical models for earthquake occurrences and residual analysis for point processes, *J. Am. Stat. Assoc.,* **83**(401), 9–27.

Ogata, Y., 1998. Space-time point-process models for earthquake occurrences, *Ann. Inst. Stat. Math.,* **50**(2), 379–402.

Omori, F., 1894. On the aftershocks of earthquakes, *J. Coll. Sci., Imp. Univ., Japan,* **7,** 111–200.

Ozawa, S. & Ando, R., 2021. Mainshock and aftershock sequence simulation in geometrically complex fault zones, *J. geophys. Res,* **126**(2), e2020JB020865.

Peng, Z. & Zhao, P., 2009. Migration of early aftershocks following the 2004 Parkfield earthquake, *Nat. Geosci.,* **2**(12), 877–881.

Perfettini, H. & Avouac, J., 2004. Postseismic relaxation driven by brittle creep: a possible mechanism to reconcile geodetic measurements and the decay rate of aftershocks, application to the Chi-Chi earthquake, Taiwan, *J. geophys. Res,* **109**(B2), doi:10.1029/2003JB002488.

Perfettini, H. & Avouac, J., 2007. Modeling afterslip and aftershocks following the 1992 Landers earthquake, *J. geophys. Res,* **112**(B7), doi:10.1029/2006JB004399.

Perfettini, H., Frank, W. B., Marsan, D. & Bouchon, M., 2018. A model of aftershock migration driven by afterslip, *Geophys. Res. Lett.,* **45**(5), 2283–2293.

Reasenberg, P. A. & Jones, L. M., 1989. Earthquake hazard after a mainshock in California, *Science,* **243**(4895), 1173–1176.

Rice, J. R., 1993. Spatio-temporal complexity of slip on a fault, *J. geophys. Res.,* **98**(B6), 9885–9907.

Richards-Dinger, Keith & Dieterich, James H. 2012. RSQSim Earthquake Simulator, *Seismol. Res. Lett.,* **83**(6), 983–990https://doi.org/10.1785/0220120105

Ross, Z. E. *et al.*, 2019b. Hierarchical interlocked orthogonal faulting in the 2019 Ridgecrest earthquake sequence, *Science,* **366**(6463), 346–351.

Ross, Z. E., Cochran, E.S., Trugman, D.T. & Smith, J.D., 2020. 3D fault architecture controls the dynamism of earthquake swarms, *Science,* **368,** 1357.

Ross, Z. E., Rollins, C., Cochran, E. S., Hauksson, E., Avouac, J. & Ben-Zion, Y., 2017. Aftershocks driven by afterslip and fluid pressure sweeping through a fault-fracture mesh, *Geophys. Res. Lett.,* **44**(16), 8260–8267.

Ross, Z. E., Trugman, D. T., Hauksson, E. & Shearer, P. M., 2019a. Searching for hidden earthquakes in Southern California, *Science,* **364**(6442), 767–771.

Ruiz, S. *et al.*, 2014. Intense foreshocks and a slow slip event preceded the 2014 Iquique M_w 8.1 earthquake, *Science,* **345**(6201), 1165–1169.

Savage, H. M. & Brodsky, E. E., 2011. Collateral damage: evolution with displacement of fracture distribution and secondary fault strands in fault damage zones, *J. geophys. Res.,* **116**(B3), doi:10.1029/2010JB007665.

Scholz, C. H., Dawers, N. H., Yu, J., Anders, M. H. & Cowie, P. A., 1993. Fault growth and fault scaling laws: preliminary results, *J. geophys. Res,* **98**(B12), 21 951–21 961.

Segou, M., Parsons, T. & Ellsworth, W., 2013. Comparative evaluation of physics-based and statistical forecasts in northern California, *J. geophys. Res,* **118**(12), 6219–6240.

Sirorattanakul, K., Ross, Z. E., Khoshmanesh, M., Cochran, E. S., Acosta, M. & Avouac, J., 2022. The 2020 Westmorland, California earthquake swarm as aftershocks of a slow slip event sustained by fluid flow, *J. geophys. Res,* **127**(11), doi:10.1029/2022JB024693.

Stein, R. S., 1999. The role of stress transfer in earthquake occurrence, *Nature,* **402**(6762), 605–609.

Stein, R. S., Barka, A. A. & Dieterich, J. H., 1997. Progressive failure on the North Anatolian fault since 1939 by earthquake stress triggering, *Geophys. J. Int.,* **128**(3), 594–604.

Tape, C. *et al.*, 2018. Earthquake nucleation and fault slip complexity in the lower crust of central Alaska, *Nat. Geosci.,* **11**(7), 536–541.

Trugman, D. T. & Ross, Z. E., 2019. Pervasive foreshock activity across southern California, *Geophys. Res. Lett.,* **46**(15), 8772–8781.

Utsu, T., Ogata, Y & Matsu'ura, R.S.,., 1995. The centenary of the Omori formula for a decay law of aftershock activity, *J. Phys. Earth,* **43**(1), 1–33.

van den Ende, M. P. A. & Ampuero, J., 2020. On the statistical significance of foreshock sequences in Southern California, *Geophys. Res. Lett.,* **47**(3), e2019GL086224, doi:10.1029/2019GL086224.

Vidale, J. E. & Shearer, P. M., 2006. A survey of 71 earthquake bursts across southern California: exploring the role of pore fluid pressure fluctuations and aseismic slip as drivers, *J. geophys. Res,* **111**(B5), doi:10.1029/2005JB004034.

Yoon, C. E., Yoshimitsu, N., Ellsworth, W. L. & Beroza, G. C., 2019. Foreshocks and mainshock nucleation of the 1999 M_w 7.1 Hector Mine, California, earthquake, *J. geophys. Res,* **124**(2), 1569–1582.

Ziv, A., 2003. Foreshocks, aftershocks, and remote triggering in quasi-static fault models, *J. geophys. Res,* **108**(B10), doi:10.1029/2002JB002318.

Ziv, A., 2006. What controls the spatial distribution of remote aftershocks?,*Bull. seism. Soc. Am.,* **96**(6), 2231–2241.

Ziv, A. & Rubin, A. M., 2003. Implications of rate-and-state friction for properties of aftershock sequence: quasi-static inherently discrete simulations, *J. geophys. Res,* **108**(B1), doi:10.1029/2001JB001219.